

**THE MULTIPLE FACETS OF
OHMIC CONFINEMENT IN ASDEX**

M. Bessenrodt-Weberpals, K. McCormick,
F. X. Söldner, F. Wagner,
H. S. Bosch, O. Gehre, E. R. Müller,
H. D. Murmann, J. Neuhauser, W. Poschenrieder,
K. H. Steuer, N. Tsois*, and the ASDEX Team

IPP III/161

August 1990



MAX-PLANCK-INSTITUT FÜR PLASMAPHYSIK

8046 GARCHING BEI MÜNCHEN

MAX-PLANCK-INSTITUT FÜR PLASMAPHYSIK

GARCHING BEI MÜNCHEN

THE MULTIPLE FACETS OF OHMIC CONFINEMENT IN ASDEX

M. Bessenrodt-Weberpals, K. McCormick,
F. X. Söldner, F. Wagner,
H. S. Bosch, O. Gehre, E. R. Müller,
H. D. Murmann, J. Neuhauser, W. Poschenrieder,
K. H. Steuer, N. Tsois*, and the ASDEX Team

IPP III/161

August 1990

Abstract

The scaling of the energy confinement time with plasma density and current has been investigated for Ohmically heated tokamak discharges in ASDEX. The major improvement $\tau_E \propto I_p$ maintained in the high density improved Ohmic confinement (IOC) regime with peaked density profiles. The peaking of the radial density profile can be brought about by reducing the axial power flow through the plasma surface thereby effecting a reduction of the edge density. Tailoring of the radiation profile with the addition of low-Z impurities e.g. neon gives access to the IOC regime under conditions where otherwise the degraded Saturated Ohmic Confinement (SOC) behavior prevails. The energy confinement time increases with current and decreases with heating power also in Ohmic discharges as shown by a statistical analysis. But with the intrinsic coupling between power and current, both relationships cancel and τ_E becomes independent of P_{OH} and I_p . The two most prominent features of Ohmic confinement can therefore be explained on the basis of simple physical models.

*N.R.C.N.S. Democritos, Athens, Greece

Die nachstehende Arbeit wurde im Rahmen des Vertrages zwischen dem Max-Planck-Institut für Plasmaphysik und der Europäischen Atomgemeinschaft über die Zusammenarbeit auf dem Gebiete der Plasmaphysik durchgeführt.

THE MULTIPLE FACETS OF OHMIC CONFINEMENT IN ASDEX

M. Bessenrodt-Weberpals, K. McCormick, F. X. Söldner, F. Wagner, H.S. Bosch,
O. Gehre, E.R. Müller, H.D. Murmann, J. Neuhauser, W. Poschenrieder,
K.H. Steuer, N. Tsois*, and the ASDEX Team

Max-Planck-Institut für Plasmaphysik, EURATOM Association,
Boltzmannstrasse 2, D - 8046 Garching, FRG

To Professor Rudolf Wienecke on his 65th Birthday

Abstract

The scaling of the energy confinement time with plasma density and current has been investigated for Ohmically heated tokamak discharges in ASDEX. The linear dependence $\tau_E \sim \bar{n}_e$ is maintained in the high density Improved Ohmic Confinement (IOC) regime with peaked density profiles. The peaking of the radial density profile can be brought about by reducing the net power flow through the plasma surface thereby effecting a reduction of the edge density. Tailoring of the radiation profile with the addition of low-Z impurities e.g. neon gives access to the IOC regime under conditions where otherwise the degraded Saturated Ohmic Confinement (SOC) behavior prevails. The energy confinement time increases with current and decreases with heating power also in Ohmic discharges as shown by a statistical analysis. But with the intrinsic coupling between power and current, both relationships cancel and τ_E becomes independent of P_{OH} and I_p . The two most prominent features of Ohmic confinement can therefore be explained on the basis of simple physical models.

* Demokritos, Attiki, Greece

1. Introduction

The confinement time is a crucial parameter for controlled nuclear fusion. The Lawson criterion states that a lower limit of the product of confinement time τ_E and density has to be surpassed for ignition and burn. The energy confinement time characterizes the heat transport processes in tokamaks which, however, are not well understood. As there is no predictive understanding from first principles, scaling studies on the basis of the existing experimental material are done to predict the expected confinement of future experiments.

For many years the dominant scaling parameter of τ_E was the plasma density. This scaling relation was based on Ohmic discharges. It had the rather beneficial aspect that the parameter in the Lawson criterion, density \times confinement time, depended quadratically on density. This relation was the basis for the INTOR study.

The leading scaling parameter changed totally in auxiliary heated discharges. There, the density is of minor importance as scaling parameter. Instead, τ_E rises with plasma current and decreases with heating power; under Ohmic conditions, there is no explicit current (or power) dependence in τ_E . The scaling results from auxiliary heated plasmas are used in the design of ITER.

In this paper we describe two elements of OH confinement which are specific to this intrinsic heating mechanism not existent under high power auxiliary heating: One is the link between the plasma current and the plasma heating power. Under OH conditions the heating is invariably connected with elements of the magnetic configuration i.e. the poloidal field or the rotational transform. The second element specific to OH heating is the low heat flux across the plasma boundary which determines the plasma edge conditions. E.g. the edge density is correlated with the power flux across the boundary which, on the other hand, is strongly varied by impurity radiation. As a consequence, the separatrix density is guided by the balance between input power and radiated power. The edge density is, as we will see, a key parameter for the density profile shape and through it to regimes with good confinement. Thus the edge density, density profile shape and

improvement in plasma energy content depend sensitively on the impurity species and its radiation characteristics.

With auxiliary heating the contribution of Ohmic power to the total power input diminishes. The proportionality between plasma current I_p and heating power disappears with increasing additional heating power. Impurity radiation increases approximately proportionally to the total input power. Thus the net heat flux into the scrape-off layer rises with increasing additional heating power, causing the edge density to rise. Therefore, methods which reduce the edge density in Ohmic discharges and allow access into good confinement regimes are applied to auxiliary heated discharges with decreasing effectiveness. In the following we will describe the consequences of the coupling between heating power and plasma current and the specific edge conditions on confinement and on the scaling of the confinement time. The experimental data are obtained from divertor discharges of ASDEX.

2. Density dependence of the energy confinement time τ_E

In ASDEX three different regimes of Ohmic confinement have been identified in gas fuelled discharges. In the Linear Ohmic Confinement (LOC) regime at low density ($\bar{n}_e < 3 \times 10^{13} \text{ cm}^{-3}$) the energy confinement time τ_E increases linearly with density. At higher densities there are two major scenarios: the SOC regime is characterized by saturation and finally a roll-over of τ_E with density, and the IOC regime shows improved Ohmic confinement where at best the linear scaling $\tau_E \sim \bar{n}_e$ continues (see Fig. 1a). The latter two regimes differ notably in the form of the density profile $n_e(r)$ (see Fig. 1b). In the SOC regime the density profile broadens with increasing line averaged density \bar{n}_e , while the transition to the IOC regime is characterized by a marked peaking of the radial density profile [1]. The IOC regime seems to continue the n_e -profile trend of the LOC regime: Also at low density, the density profile peaks with increasing \bar{n}_e .

The predominant parameter which changes in the LOC regime with density is Z_{eff} . A strong Z_{eff} variation is observed even under the best wall conditions with boronization. For carbonized wall conditions Z_{eff} scales in the LOC regime with density in a power law $Z_{\text{eff}}^{-1} \propto \bar{n}_e^\alpha$ with $\alpha = -1.16$ and Z_{eff} drops from 3-6 for $\bar{n}_e \leq 1 \times 10^{13} \text{ cm}^{-3}$ to 1-2 at $\bar{n}_e > 3 \times 10^{13} \text{ cm}^{-3}$. The electron temperature also decreases with increasing density

whereas the T_e -profile shape is rather invariant. As a consequence, the Ohmic power input ($\propto Z_{\text{eff}} \times f(Z_{\text{eff}}) \times T_e^{3/2} \times I_p^2$) is fairly independent of \bar{n}_e , i.e. $P_{\text{OH}} \propto \bar{n}_e^{0.26}$. Because of the strong Z_{eff} variation the energy content of the ion component increases strongly. W_i is calculated from the ion energy balance using a multiplier to the neoclassical ion heat conductivity which is matched to the measured central ion temperature T_{i0} . It scales strongly with density as: $W_i \propto \bar{n}_e^{0.83}$. The electron energy content measured from Thomson scattering, varies as $W_e \propto \bar{n}_e^{0.38}$. The total energy content W_{tot} is determined from the average of equilibrium, diamagnetic and kinetic β_{pol} , with I_i determined from the T_e -profile and W_i as described above. The density scaling gives $W_{\text{tot}} \propto \bar{n}_e^{0.77}$. Figure 2 shows these three density dependencies of the total, the electron and the ion energy content. It is clear from this figure that the pronounced density dependence of W_i - led by the decrease of Z_{eff} - contributes to a substantial part to the density scaling of τ_E in the low-density LOC regime. Nevertheless, there still remains a density dependence, observed in W_e in addition to the increase of W_i with \bar{n}_e . The residual \bar{n}_e variation may be due to the peaking of the $n_e(r)$ profile.

At the transition into the IOC regime, the profile modification starts with a decrease of the edge density as a corollary to the reduction of the external gas flux to the level necessary to sustain flat top phases at high density. The peaking factor $n_e(0)/\langle n_e \rangle$ rises with \bar{n}_e in the IOC regime. Pellet injection at high density leads to a similar evolution of the discharge as the IOC transition. The peaking of the density profile correlates in both cases with an improvement of the energy confinement time, and the recovery of the linear scaling $\tau_E \sim \bar{n}_e$. Transport code calculations have shown that degradation and improvement in confinement can be consistently explained by excitation and suppression of η_i -modes due to flattening or steepening of the density gradient, respectively [2].

3. Role of the edge conditions for the attainment of the IOC regime

The IOC regime on ASDEX was found after a modification of the divertors which resulted in a higher impurity level, increased recycling and

concomittantly a reduced gas consumption. The gas puff fuelling rate dropped by a factor of two. Improved Ohmic Confinement appeared during density plateaus above the LOC region. The transition from SOC to IOC was triggered by the sharp drop of external gas flux associated with the transition from a density ramp to a density plateau.

The improvement in energy confinement depends on the wall conditions. The highest values, extending the linear scaling $\tau_E \sim \bar{n}_e$ up to the density limit, were obtained with uncovered stainless steel walls and with carbonization in a mixture of deuterized methane and nitrogen and subsequent glow discharge conditioning. The discharges in these cases had a high level of radiation. With clean walls after fresh carbonization or boronization or with hydrogen as working gas nearly no enhancement of τ_E above SOC values was obtained. In these cases also the density profile remained flat (see Figure 1). In the course of several experimental periods with various wall conditions the whole range in τ_E between the best IOC values and the SOC boundary was covered. Close correlation was found between the improvement in confinement and the relative drop in the external gas puffing rate at the beginning of high density flat top phases [3]. A sudden cut of the gas fuelling rate gave rise to a decrease of the edge density. This suggested that a critical reduction of the electron density at the plasma edge is required in order to start the steepening of the density gradient in the confinement region. With shortening of the density decay length L_n the parameter $\eta_i = L_n/L_{Ti}$ can fall below the threshold value for excitation of ion pressure gradient driven modes. These so-called η_i -modes are considered to be responsible for the confinement degradation in the SOC regime. Suppression of these modes may then give access to the IOC regime [4].

4. Edge modelling

We will go into some detail with the discussion of the applied edge model and measured parametric dependences observed at the edge of ASDEX plasmas. The insight into the physics governing the plasma edge, allows us to understand and highlight aspect which ultimately affects bulk confinement and - in particular - interpret the special circumstances of Ohmic confinement.

There is no evidence for the view that the IOC regime represents an anomaly in terms of edge plasma physics (e.g. like the formation of the thermal edge barrier in the H-mode [5]). Although the edge density is strongly reduced in IOC discharges, the physical processes governing the edge remain about the same during *all* Ohmic confinement regimes, i.e. LOC, SOC and IOC [6]. One prominent example is the correlation between the electron temperature T_{es} and the electron density n_{es} at the separatrix which follows roughly the global scaling $T_{es} \sim n_{es}^{-0.4}$, taken from 88 % minor radius [7], with a marginal deviation to smaller values for the IOC data. Numerical simulations with a one-dimensional hydrodynamic code for the charged particles coupled to a Monte-Carlo code for the neutral species [8] are also in qualitative agreement with these experimental findings as it can be seen in Figure 3. Here, the code values are increased by a factor of 2 to take into account that the nominal separatrix position (determined by the plasma equilibrium based on magnetic probes and measured with an accuracy of ± 1 cm at the outer midplane) is about 1 cm further inside the plasma than what we believe is the true separatrix position. The actual separatrix position is deduced from pressure balance and correlation measurements on fluctuations in the scrape-off layer between midplane and divertor plasma as measured by Langmuir probes [9]. The such determined separatrix agrees with additional studies of the intersection point of energetic electrons with a movable target which penetrates the plasma at the outer mid-plane. To motivate a physical understanding of the empirical scalings within the edge parameters, we consider a standard classical heat flow model along field lines with simplified source treatment in order to justify an analytical model for the edge plasma. This is based on the one-dimensional heat conductivity equation without any source term [10]

$$\frac{\partial}{\partial s} \kappa_{\parallel} \frac{\partial}{\partial s} T_e = 0 \quad (1)$$

along open field lines (coordinate s) in the Scrape-Off Layer (SOL) plasma with $\kappa_{\parallel} = \kappa_0 T_e^{5/2}$ taken from Spitzer's law. The power input and the divertor and target losses are accounted for by boundary conditions in the midplane ($s = 0$) and at the target plate ($s = L_0$), i.e. we include the power input

$$-\kappa_{||} \frac{\partial}{\partial s} T_e = P_{sol}/A_{sol} \quad (2)$$

across the SOL surface A_{sol} at the separatrix ($s = 0$) and the power deposition

$$-\kappa_{||} \frac{\partial}{\partial s} T_e = n_e (\delta k_B T_e + E_{ion}) v_{||} + P_{rad, div} / A_{sol} \quad (3)$$

at the divertor plates ($s = L_c$), which are coupled along the connection length L_c . The input power P_{sol} consists of the total heating power P_{tot} minus the total radiation losses in the main chamber $P_{rad, main}$ (bulk and boundary plasma), but not in the divertor chamber:

$$P_{sol} = P_{tot} - P_{rad, main}$$

The divertor radiation $P_{rad, div}$ reduces the power in the divertor chamber P_{div} which is deposited onto the target plates:

$$P_{div} = P_{sol} - P_{rad, div}$$

Since the decay length remains about the same, A_{sol} is also practically constant during all scenarios. The energy transfer factor δ is calculated by kinetic simulations to be $\delta \approx 8$; the effective hydrogen ionization energy E_{ion} takes stepwise ionization processes into account. The solution of the model equations (1) - (3) gives the temperature distribution

$$(T_e(s))^{7/2} = T_{es}^{7/2} - \frac{7}{2} \frac{P_{sol}}{A_{sol} \kappa_0} s \quad (4)$$

along field lines with the separatrix temperature $T_{es} = T_e(0)$ as the starting value and the divertor temperature $T_{ed} = T_e(L_c)$ as the final value. The pressure decay along open field lines is calculated from the momentum balance. Assuming Mach numbers $M(0) = 0$ at the separatrix and $M(L_c) = 1$ at the sheath yields

$$n_{es}T_{es} = 2 n_{ed} T_{ed} \quad (5)$$

Equations (4) and (5) finally determine the separatrix density n_{es} from

$$n_{es}T_{es} \sqrt{T_{ed}} \left(1 + \frac{E_{ion}}{\delta k_B T_{ed}} \right) = \sqrt{\frac{2\pi m_i}{k_B^3}} \frac{2}{A_{sol} \delta} (P_{div}) \quad (6)$$

and hence also the divertor density n_{ed} .

Far away from the density limit equation (6) yields

$$T_{es} \propto n_{es}^{-2/3} \times P_{div}^{2/3}$$

which agrees quite well with the empirical scaling (based on the measured P_{sol}):

$$T_{es} = 92 n_{es}^{-0.77 \pm 0.04} \times P_{sol}^{0.65 \pm 0.03} \quad R=0.94$$

obtained from the data base of Fig. 4. (R is the regression coefficient)

The behavior of edge parameters in Ohmic heating scenarios differs from additional heating with regard to two aspects. During auxiliary heating scenarios the edge parameters are largely independent of the small amount of Ohmic power. Further, as $n_{es}T_{es}$ depends on the absolute value of the power flow into the SOL, radiation losses have a larger effect on OH discharges. Since P_{sol} consists of the difference between P_{OH} and $P_{rad,main}$, one may also influence P_{sol} by the addition of impurities or by changing wall conditions (carbonization vs. boronization).

The strong dependence of both P_{OH} and P_{div} on the impurity content in Ohmic plasmas leads to a rather complicated dependence of the plasma energy content on the dominant impurity species: High-Z impurities increase the plasma resistivity and thereby increase the Ohmic power input (at constant plasma current), but also enhance the central radiation. The net flux across the separatrix can be decreased as well as increased. Low-Z impurities, on the other hand, may lead to a moderate increase of Ohmic power, but to a pronounced reduction of the input SOL power if strong line radiation occurs close to the edge and in the SOL.

Unlike central radiation, edge radiation does not strongly decrease the plasma energy content but modifies the plasma edge conditions. Such a sensitivity on the impurity species is not observed during auxiliary heating in the L-mode. Furthermore, the specific wall conditioning influences the plasma behavior under Ohmic conditions. Since boronization strongly reduces the radiation level, the power influx into the SOL is larger in this case than for carbonized conditions.

We have tested the fundamental relation between edge parameters and net power flux within the SOL as given by equ. (6) in a power scan with neutral beam injection. The total heating power was varied from 0.25 - 1.8 MW; \bar{n}_e was varied in the range $2.0 \leq \bar{n}_e (10^{13} \text{ cm}^{-3}) \leq 5.5$. Figure 4 gives the left hand side of equ. (6) as a function of P_{SOL} with \bar{n}_e as parameter. Measurements of both the edge and the divertor parameters were available. Equation (6) appears to describe the situation well in spite of the apparent scatter for $P_{\text{SOL}} > 1$ MW which may be attributed to a changing SOL width..

Figure 5 shows basically the same relation of equ. (6) but now only for Ohmic heating. As the divertor temperatures were not measured in the scans of Fig. 5 we simply plot the edge pressure. Results from hydrogen and deuterium plasmas are given. The net power input into the SOL was varied in the Ohmic scan by current, toroidal field, and density. Again a linear dependence between edge pressure and net power flux is obtained, confirming relation (6) also for Ohmic conditions.

The above edge model, with the power flux through the SOL as the key element was also applied to the various Ohmic confinement regimes in ASDEX to test the consistency within the edge data. For each value of the separatrix temperature and the power flux into the SOL to the divertor plates, we calculate the separatrix density. The theoretical results agree reasonably well with the experimental observations as shown in Figure 3. Moreover, the importance of the power influx P_{SOL} into the SOL highlights the role of the impurities in Ohmic plasmas. The IOC regime cannot be reached under boronized conditions where the oxygen level is strongly reduced and the total radiation losses are rather small. Obviously, clean conditions lead to a high power flux across the separatrix and hence to a high edge pressure which is unfavorable for improved confinement. It thus seems that IOC conditions need a certain

amount of light impurities in order to keep the power influx into the SOL at a low level. This may explain why IOC was first achieved in ASDEX after the divertor bypasses were opened such that the global recycling increased. The recycling flux from the divertor through e.g. the bypasses is polluted by impurities, typically by a few percent of CO which provides sufficient radiation. When in successive steps the divertor bypasses were closed again, the accessibility of the IOC regime was reduced. This may also explain why IOC is restricted to deuterium discharges, where the radiation level is higher. Under boronized conditions in the SOC regime the following relation for the total radiation power is observed: $P_{\text{rad}} \sim A^{0.53 \pm 0.04}$. Moreover, it may become evident why IOC conditions cannot be established in clean plasmas with boronized walls where the radiation level is strongly reduced.

5. Studies with impurity injection

With the experience of the close link between confinement improvement and the wall conditions and with the results of the plasma edge modelling in mind, we performed a series of experiments where small amounts of various impurity gases with different Z values were added to the main working gas deuterium. For regular studies of the different Ohmic confinement regimes under various operating conditions a special type of plasma discharge had been tailored. Transitions between all confinement regimes are documented in a single discharge [4] with three density flat top phases in the regions of LOC and SOC/IOC and density ramps in between.

This type of discharge was used also to study the influence of impurity radiation on confinement. We firstly perform discharges with moderate impurity puffing of various gases in order to properly choose the most efficient impurity gas for puffing. The rare gases neon, argon and krypton were injected in short pulses during the density ramps between 0.5 - 0.8 s and 1.5 - 1.7 s, respectively (see Figure 6). During the subsequent flat top phases their concentration in the plasma decreases only slowly due to the high recycling coefficient. Nitrogen which has a low recycling coefficient was injected at a low flow rate during the

whole discharge. Nitrogen and neon have low Z values of 7 and 10, respectively, the heavier gases argon and krypton $Z = 18$ and 36, respectively. Bolometric measurements yield radiation profiles of nitrogen and neon which peak in the plasma periphery, as it is the case for oxygen - the intrinsic impurity, whereas the dominant argon and krypton lines are most prominent further inside. Thus, the peripheral radiation losses for the low- Z elements combine the favorable situation of a small energy loss in the main plasma with a low power deposition to the divertor plates. The power flux into the SOL during the three different density plateaus, i.e. 2.7 , 4.0 , and $5.4 \times 10^{13} \text{ cm}^{-3}$, is plotted in Figure 7 for discharges in pure hydrogen, in pure deuterium with SOC conditions in the density plateaus, in deuterium with additional small amounts of neon, and for a discharge in deuterium where the IOC has developed. Obviously, the discharge with additional neon puffing reaches quite a low power into the SOL which amounts to 280 kW at $2.7 \times 10^{13} \text{ cm}^{-3}$ and 200 kW at $5.4 \times 10^{13} \text{ cm}^{-3}$. The reduced power flux is corroborated by the calorimetric measurements of the deposited energy at the divertor plates. The lowest level of power deposition onto the divertor plates is obtained with neon puffing.

We then proceed with a second series of discharges where we concentrate on neon puffing and try to optimize the impurity amount. In these cases, neon contributes a few percent to the total particle fluxes which is indeed comparable to the CO contamination of the recycling gas during the IOC discharges of the open divertor. We thus achieve discharge conditions which are almost identical to IOC conditions. This comprehends many aspects. In Figure 6 the evolution of various plasma parameters is compared for three discharges with different wall conditions. The discharge #24707 with uncovered stainless steel walls gives typical IOC transitions. The discharge #30451 with boronized walls remains in the SOC regime at high density. In discharge #30687 with boronized walls (as #30451) additional neon puffing is applied from 0.5 - 0.8 s and with higher flux between 1.5 - 1.9 s. The neon-puffing yields high energy confinement times of up to $\tau_E \approx 120 \text{ ms}$ like in the IOC discharge #24707 at the highest density. In both discharges with IOC transitions the improvement of the confinement time is correlated with peaking of the density profile. This is seen from the increase of the ratio

of the HCN interferometer signals from the central channel and the channel at $r/a = 0.75$ plotted in the second slot of Figure 6. The Ohmic power input given in the third row is slightly increased during neon injection. But after cutting off the neon puff the Ohmic power decreases and beta increases to values comparable with the IOC reference discharge #24707. The same holds for the loop voltage, since the plasma current is kept constant. The correlation of the confinement time τ_E with density \bar{n}_e is shown in Figure 8 for the three IOC test discharges during the time interval 0.5-2.5 s when the density is increased to three flat top phases with intermediate ramps. SOC behavior is found for the discharge #30451; neon injection in the discharge #30687 gives rise to an IOC behavior as in the reference discharge #24707. The net power flux P_{sol} into the SOL is quite low in both IOC discharges which can be seen in Figure 9. Here, the radiation losses overcome 50 percent of the Ohmic input power whereas the pure deuterium discharge with boronized walls radiates only about 20 percent of its Ohmic heating power away. This high edge radiation results in a low power load at the target plates and simultaneously a small energy loss in the bulk plasma. Moreover, the flux of neutrons attains the same high value of 5×10^{10} neutrons s^{-1} for the IOC and the neon puffed discharge at the highest density plateau compared to 3×10^9 neutrons s^{-1} with boronized walls and without any impurity puffing (cf. Figure 10).

As a prominent example of edge data, the separatrix temperature is shown for the reference (#24707) and the neon puffed (#30687) IOC in Figure 11 in comparison with the pure deuterium case (#30451). The picture reveals that the typical IOC features with moderate depression in the separatrix temperature as given in [6] are now found again under boronized conditions with optimized neon puffing. In addition, the divertor data like the line-integrated electron density, which is determined by microwave interferometry, or the neutral gas pressure as given by ionization gauges show the IOC signatures: The values are much lower in the (IOC) density plateaus than in the SOC density ramps during the discharges with strong neon puffing. This confirms our ideas about the critical role of the power influx into the SOL for Ohmic plasmas under various wall conditions.

The form of the density and temperature profiles is similar for the

high density phase when the confinement times become comparable in the discharge with neon puffing and in the reference IOC case. This shows again the primordial importance of the form of plasma profiles, especially the density profile, for the global energy confinement. It confirms our idea that the confinement can be improved with the peaking of the density profile. This was attributed to the suppression of ion pressure gradient driven modes as shown by transport calculations [2]. The critical parameter for the excitation of these modes is the ratio of the decay lengths of density L_n and temperature L_T : $\eta = L_n/L_T$. Theory expects the critical value for the onset of ion pressure gradient driven turbulence between 1 and 2. The parameters η_e and η_i show similar behavior in IOC discharges [10]. Radial profiles for the parameter $\eta_e = L_{n_e}/L_{T_e}$ are determined from the well documented electron density and temperature profiles. The values of η_e decrease towards the periphery. The radius at which $\eta_e = 1.5$ is reached is plotted in Figure 12 for the three discharges discussed. The region between the plasma edge and the line of $\eta_e = 1.5$ should be stable. This region starts expanding over the whole plasma cross section in the high density phase both in the reference IOC discharge and in the discharge with neon injection. Therefore in both cases the reduction in edge density triggers a steepening of the density profile which may then potentially allow for stabilization of η_i -modes.

6. The coupling between current and heating power in Ohmic discharges

Under Ohmic conditions the heating power depends on current and is not an independent parameter as with auxiliary heating. If I_p , B_t , \bar{n}_e , the isotope mass A_i and Z_{eff} (from bremsstrahlung) are taken as independent parameters, the following scaling is obtained for carbonized (C) and boronized (B) wall conditions in the SOC regime:

$$\text{C: } P_{OH} = 7.9 \times 10^{-4} \times I_p^{1.09 \pm 0.03} \times B_t^{-0.40 \pm 0.06} \times \bar{n}_e^{0.24 \pm 0.04} \times A_i^{-0.22 \pm 0.03} \quad (R = 0.96)$$

$$\text{B: } P_{OH} = 5.6 \times 10^{-4} \times I_p^{1.13 \pm 0.02} \times B_t^{-0.35 \pm 0.03} \times \bar{n}_e^{0.26 \pm 0.02} \times$$

$$A_i^{-0.18 \pm 0.01} \quad (R = 0.99)$$

The external parameters have been varied within the following ranges:

$$C: \quad .8 \leq \bar{n}_e \text{ (} 10^{13} \text{ cm}^{-3} \text{)} \leq 5.5$$

$$.15 \leq I_p \text{ (MA)} \leq .44$$

$$1.9 \leq B_t \text{ (T)} \leq 2.45$$

$$B: \quad 2.7 \leq \bar{n}_e \text{ (} 10^{13} \text{ cm}^{-3} \text{)} \leq 5.5$$

$$.25 \leq I_p \text{ (MA)} \leq .45$$

$$1.9 \leq B_t \text{ (T)} \leq 2.8$$

The loop voltage is found to be basically independent of plasma current as can be seen from the close to linear variation of P_{OH} with I_p . The effect of an increase of I_p is offset in the loop voltage by the simultaneous increase of the electrical conductivity σ owing to the rise of the electron temperature with current. The leading term in the increase of σ is, however, not so much the central temperature ($T_{e0} \propto I_p^{0.31}$ (C), $\propto I_p^{0.29}$ (B)) but the effect of I_p on the temperature profile ($\langle T_e \rangle \propto I_p^{0.85}$ (C), $\propto I_p^{0.96}$ (B)).

Both the total and the electron energy content W_{tot} and W_e increase linearly with current. The regression analysis yields the following results in the SOC regime.

$$C: \quad W_{tot} = 5.7 \times 10^{-2} \times I_p^{0.99 \pm 0.03} \times B_t^{-0.13 \pm 0.06} \times \bar{n}_e^{0.43 \pm 0.05} \times Z_{eff}^{-0.16 \pm 0.05} \times A_i^{0.28 \pm 0.03} \quad (R = 0.97)$$

$$B: \quad W_{tot} = 1.6 \times 10^{-2} \times I_p^{1.19 \pm 0.04} \times B_t^{-0.32 \pm 0.07} \times \bar{n}_e^{0.44 \pm 0.05} \times A_i^{0.47 \pm 0.03} \quad (R = 0.98)$$

Also in the LOC regime P_{OH} and W_{tot} scale with current : $P_{OH} \propto I_p^{1.02}$, $W_{tot} \propto I_p^{1.12}$ (C).

Figure 13 shows the data of W_{tot} , P_{OH} and their ratio, τ_E , against the scaling results for SOC conditions. The scattering of energy and power data points is low because of the current as dominant scaling parameter. The confinement time data, however, show a high scattering as the

leading scaling parameter I_p cancels and secondary effects determine the scatter in the scaling of τ_E . The obvious improvement of the energy content with current is offset in the confinement time of Ohmically heated plasmas by the degradation with the power [11]. Under Ohmic conditions current and power dependences just cancel in the τ_E scaling. With auxiliary heating, power and current are not linked any longer and it becomes evident that current improves and heating power degrades confinement.

With auxiliary heating W_{tot} scales typically $\propto P^\alpha \times I_p^\beta$. Because of the proportionality between P_{OH} and I_p , $\beta \approx 1 - \alpha$ under Ohmic conditions. In the publications on beam heating, α scatters around 0.5 while β is in the range 0.5 - 1.2. On ASDEX we observed in a detailed current scan with auxiliary heating for boronized wall conditions the relation: $W_{tot} \propto I_p^{0.77 \pm 0.03} \times P_{tot}^{0.35 \pm 0.08}$ (in the range $2.7 \leq \bar{n}_e (10^{13} \text{ cm}^{-3}) \leq 5.5$). The auxiliary heating power was kept constant at $P_{NI} = 1.6 \text{ MW}$ at a level where the remaining Ohmic input power could be neglected. The power dependence is obtained from the comparison of Ohmic data and those with beam heating. Other sets of power and current scans under L-mode conditions in various campaigns yield the dependence: $W_{tot} \propto I_p^{0.45 \pm 0.07} \times P_{tot}^{0.36 \pm 0.03}$ ($0.29 \leq P_{NI}(\text{MW}) \leq 1.34$). With auxiliary heating the relation $\alpha + \beta = 1$ is not so strictly maintained any longer as under Ohmic conditions.

Figure 14 plots the energy content versus current for specific scans performed to elucidate the nature of current scaling in greater detail. Data are taken under steady state conditions and, in order to study details, with slowly increasing current (from .25 MA to .45 MA within 2.2 s). W_{tot} rises linearly with current under Ohmic conditions. With auxiliary heating W_{tot} versus I_p behaves more in the form of a linear offset relation which translates into a current dependence of $W_{tot} \propto I_p^\alpha$ with $\alpha < 1$. This dependence is observed both under steady-state and transient conditions. The transient current scan reveals details in the W_{tot} versus I_p dependence which cannot be described by a simple off-set linear or power law ansatz. Nevertheless, these additional effects (e.g. the role of sawteeth at low q_a) which are not controlled in the studies presented here, may render the current scaling somewhat differently under Ohmic

and NI conditions.

The electron energy content is one constituent of W_{tot} and it is diagnostically accessible with high precision. W_e depends on I_p both under Ohmic and NI heating conditions: $W_e \propto I_p^{1.17 \pm 0.01}$ (OH) and $W_e \propto I_p^{0.88 \pm 0.02}$ (NI). The close to linear dependence of W_e is to a large extent the actual origin of the current scaling of τ_E . Like in the Ohmic case the leading term behind the current scaling of W_e is that of the average electron temperature $\langle T_e \rangle$ ($\langle T_e \rangle \propto I_p^{0.83 \pm 0.02}$) and not the central temperature T_{e0} ($T_{e0} \propto I_p^{0.27 \pm 0.03}$). In summary, we find similar current scalings of the basic constituents of W_{tot} , v.i.z. $\langle T_e \rangle$ and W_e irrespective of the heating method.

In the following table, we present the individual exponents of current (α) and power (β) from a combined analysis of the Ohmic and beam heating data (with boronization) and compare them with those of the current (or power) for the Ohmic subset.

	α	OH+NI β	$\alpha+\beta$	OH α
W_{tot}	0.69	0.47	1.16	1.19
W_e	0.8	0.29	1.09	1.17
τ_E	0.84	-0.71	0.13	0.00
$T_{e0}^{1)}$	0	0.33	0.33	0.29
$\langle T_e \rangle$	0.68	0.28	0.96	0.96

1) No significant I_p scaling is observed if the regression analysis includes OH and NI data with P_{tot} as an independent parameter.

The comparison shows that the sum of I_p and P_{tot} exponents obtained from Ohmic and NI data agree well with the exponent for current (or power) scaling under Ohmic conditions alone. It further indicates how the Ohmic current scaling of the listed parameters actually is the combined result from a heating and a current term. This is particularly documented by the way power and current scaling cancel in τ_E for Ohmic discharges.

The results from the regression analysis in the various regimes are summarized in Table 1.

7. The density variation of Ohmic power input

We have identified the power as a degrading agent of confinement also under Ohmic conditions in ASDEX. Therefore, the density dependence of the Ohmic input power remains to be investigated, especially the extent to which it affects the density (or lack of density) dependence of τ_E . Figure 15 shows the density variation of P_{OH} for various currents. Only the fit-results are given for clarity. For the 250 kA case, the individual data points are also shown.

The Ohmic input power shows a rather complicated density dependence: At medium current, P_{OH} is rather insensitive to \bar{n}_e , at high current, it decreases, at low current it increases. For medium to high current, there is a minimum in the neighborhood of the LOC to IOC transition. Under IOC conditions, P_{OH} first remains constant at the LOC level and starts to rise at higher density. Though the variation of P_{OH} with current is much larger than that with density, nevertheless, a separate regression, which includes the power input as independent parameter, should modify the density scaling. The following results are obtained for carbonized walls:

$$\text{SOC: } \tau_E = 4.8 \times 10^{-2} \times I_p^{1.00 \pm 0.15} \times P_{OH}^{-0.94 \pm 0.13} \times B_t^{-0.20 \pm 0.07} \times n_e^{0.44 \pm 0.05} \times A_i^{0.43 \pm 0.03} \quad (R = 0.91)$$

$$\text{LOC: } \tau_E = 3.6 \times 10^1 \times I_p^{1.47 \pm 0.09} \times P_{OH}^{-1.37 \pm 0.08} \times B_t^{-0.33 \pm 0.08} \times n_e^{0.69 \pm 0.03} \times A_i^{0.18 \pm 0.03} \quad (R = 0.93)$$

The density dependence in the SOC regime is stronger if P_{OH} is included ($\bar{n}_e^{0.26}$ without P_{OH}). Without explicit incorporation of P_{OH} in the LOC regime the regression coefficient is 0.8 instead of 0.93. The density allows a slight variation of P_{OH} at constant I_p . Though the variation margin is small and the errors in the exponents are high, nevertheless the sum of the exponents of P_{OH} and I_p is approximately zero.

It is interesting to compare in this context the density scaling of τ_E with Lower Hybrid instead of OH heating. In order to emulate an OH

density scan where the loop voltage is adjusted by the feedback-system such that I_p remains constant, we have varied the LH power for constant current such that the loop voltage remained zero i.e. the total plasma current is driven by the Lower Hybrid waves. In this case, due to the density dependence of the current drive efficiency, the LH power increases proportionally to \bar{n}_e . The density dependence of τ_E (thermal) is then found to be strongly reduced.

8. Discussion

The success of achieving the IOC regime in ASDEX with neon puffing under otherwise clean wall conditions reminds one of experiments in other machines where a close correlation between improved confinement and impurity injection also was found.

Ohmic deuterium discharges in PLT where large amounts of neon were puffed in are characterized by higher central electron temperatures and longer electron energy containment times than regular discharges. The authors [12] ascribe this improvement to the increase in Z_{eff} and hence to the higher Ohmic heating power input. Contrary to the PLT results, the central $Z_{\text{eff}}(0)$ in ASDEX is only moderately increased with neon puffing from about 1.5 to 2. Thus the Ohmic power input changes only slightly in these discharges.

In ISX-B, chromium gettering has been performed to achieve clean wall conditions. But with neutral beam injection gettered plasmas showed a lower energy content than ungettered ones. Therefore, some low-Z impurities were added. Non-recycling impurities such as C from methane or S from silane give no enhancement, but an improvement in both the global energy and particle confinement time has been achieved with neon puffing. As stated by Lazarus et al. [13], a cold plasma mantle is built up by radiative cooling in the edge. This scenario establishes a favorable boundary condition and yields e.g. a peaking of the radial density profile. In contrast, τ_E and τ_p both decrease in Ohmic plasmas if neon is added and simultaneously the radial density profile becomes less peaked.

Strong correlation between the confinement and the impurity content was also found in Ohmic discharges in T-10 [14]. Improved

confinement in the so-called B-regime was attained only in conditions of high radiation level. After fresh carbonization and with low impurity influx the discharges remained in the S-regime of low confinement. With additional neon puffing the transition to improved confinement could be triggered similarly to the experiments on ASDEX described in this paper.

It is also clear from our studies on the mechanisms which guarantee low edge density and thereby provide the IOC conditions why intensive limiter conditioning is necessary for maintaining peaked density profiles in limiter tokamaks like in the TFTR supermode. An interesting additional aspect could be that intense conditioning provides sufficient carbon which contributes to strong edge radiation.

The confinement time scaling on ASDEX in the LOC regime ($\bar{n}_e \leq 2.5 \times 10^{13} \text{ cm}^{-3}$) is not in agreement with the results from other tokamaks where a q_a -scaling in τ_E in addition to the usual \bar{n}_e -scaling is reported. The outcome of our study - the cancellation of P_{OH} and I_p in τ_E - applied to an experiment with distinct q_a scaling can only be reconciled if there is a stronger than linear variation of P_{OH} with I_p . This cannot be ruled out in particular as impurity composition varies from experiment to experiment. We speculate, however, that the q_a dependence seen in other experiments is actually a Z_{eff} dependence as we observe it on ASDEX at low density ($\tau_E \propto Z_{eff}^{-0.31}$). It is interesting to note that we recover a slight q_a -dependence ($\tau_E \propto q_a^{0.25}$) if we replace independently measured Z_{eff} values from bremsstrahlung radiation by the one deduced from the Spitzer relation.

9. Summary

The confinement behavior of Ohmically heated tokamak discharges has been analyzed for a wide range of operating conditions on ASDEX. The linear increase of confinement time with density $\tau_E \sim \bar{n}_e$ in the LOC regime is mainly explained by a decrease of Z_{eff} and therefore an increase of the ion energy content with rising density. At higher density where ion heat conduction starts to play a role (on ASDEX for $\bar{n}_e > 3 \times 10^{13} \text{ cm}^{-3}$) we achieve either the degraded SOC regime or the IOC regime with

improved confinement where the scaling $\tau_E \sim \bar{n}_e$ prevails up to the density limit. The improvement in confinement correlates with peaking of the density profile $n_e(r)$ which may then allow for stabilization of ion pressure gradient driven modes governing anomalous ion heat conduction losses. The peaking of the radial density profile is triggered by a reduction of the edge density following the reduction of the external gas flux. However, this becomes only effective if additionally the edge radiation is high. According to model calculations on edge and divertor plasma parameters, the separatrix density is lower if the net power flow through the plasma surface $P_{\text{tot}} - P_{\text{rad}}$ is reduced. Thus, the IOC regime is only accessible with low-Z impurities which radiate from the periphery and reduce the power flux across the separatrix. In case of very clean discharges additional injection of impurities modifies the power balance and allows in fact a transition into the IOC regime. With neon injection the net power flow $P_{\text{OH}} - P_{\text{rad}}$ was minimized thereby. With the resulting drop in edge density a transition from the SOC to the IOC regime can be triggered, resulting in an increase of the confinement time from $\tau_E \approx 75$ ms to $\tau_E \approx 120$ ms. With additional heating the net power flow and consequently the edge density increase. Reducing the separatrix density then has less influence on the shape of the density profile and no improvement in confinement is obtained any longer from peaking of the radial density profile. This would explain why regimes of improved confinement with peaked density profiles are accessible only at relatively low heating power, and the density dependence of the confinement time is lost with strong additional heating.

The other striking feature of Ohmic confinement is the lack of current dependence as it is usually found in experiments with additional heating. A statistical analysis on a large data base of Ohmic discharges on ASDEX in the LOC and SOC regimes of parameters which ultimately determine τ_E reveals clearly that also under Ohmic conditions power and current separately govern confinement. The same coefficients for scaling of W_{tot} , W_e , its constituents T_{e0} and $\langle T_e \rangle$ and τ_E with P_{tot} and I_p are found for Ohmic and beam heated plasmas. But with the intrinsic coupling between P_{OH} and I_p in Ohmic discharges the two functional dependencies cancel in first order and τ_E becomes independent of I_p . With additional

heating the link between plasma current and heating power is broken and both determine independently of each other the confinement time. From this point of view, the L-mode confinement is just the continuation of the SOC regime physics towards higher power.

We have tried to exemplify the multiple facets of Ohmic confinement:

It can be studied in a wide density and current range.

Thereby, the impurity content and composition are varied in a complicated fashion. The resulting Z_{eff} varies the energy content of the ions (at given n_e) and the ohmic power input. Impurity radiation affects the energy content in case of high-Z impurities; low-Z impurities give rise to edge radiation which governs the density profile shape.

All parameters - dilution, power input, core radiation and the density profile shape are found to affect confinement.

Because of the strong and rather involved role of impurities the detailed nature of Ohmic confinement should be machine specific and should scatter from experiment to experiment.

In the L-mode at higher power fluxes the role of impurities is expected to disappear and indeed a more unique behavior is observed.

References

- [1] Söldner, F.X., E.R. Müller, F. Wagner, et al., *Phys. Rev. Lett.* **61** (1988) 1105.
- [2] Fussmann, G., O. Gruber, H. Niedermeyer, et al., 12th Int. Conf. on Plasma Physics and Controlled Nuclear Fusion Research, Nice, 1988 (IAEA, Vienna, 1989) **1**, 145.
- [3] Verbeek, H., W. Poschenrieder, J.K. Fu, et al., *Plasma Phys. Controlled Fusion* (submitted, 1990).
- [4] Söldner, F.X., H.U. Fahrbach, O. Gehre, et al., 16th European Conference on Controlled Fusion and Plasma Physics, Venice (1989) *Euro-phys. Conf. Abstr.* **13B/1** (1989) 187.
- [5] Wagner, F., G. Fussmann, T. Grave, et al., *Phys. Rev. Lett.* **53** (1984) 1453.
- [6] Bessenrodt-Weberpals, M., A. Carlson, G. Haas, et al., *Plasma Phys. Controlled Fusion* **32** (1990) 21.
- [7] Kaufmann, M., W. Sandmann, M. Bessenrodt-Weberpals, et al., *Plasma Phys. Controlled Fusion* (in press, 1990).
- [8] Schneider, W., J. Neuhauser, G. Haas, et al., *Contrib. Plasma Phys.* **28** (1988) 387.
- [9] Neuhauser, J., M. Bessenrodt-Weberpals, B.J. Braams et al., *Plasma Physics Controlled Fusion* **31** (1989) 1551.
- [10] Wagner, F., and K. Lackner: Divertor tokamak experiments, in: D. E. Post and R. Behrisch (eds.): *Physics of plasma-wall interactions in controlled fusion*, London: Plenum Press (1986) pp.931.
- [11] Niedermeyer, H., F. Wagner, G. Becker et al., 11th Int. Conf. on Plasma Physics and Controlled Nuclear Fusion Research, Kyoto, 1986 (IAEA, Vienna, 1987) **1**, 125.
- [12] Meservey, E., M. Bitter, C. Daughney, et al., *Nucl. Fusion* **24** (1984) 3.
- [13] Lazarus, E. A., J. D. Bell, C. E. Bush, et al., *Nucl. Fusion* **25** (1985) 135.
- [14] Alikaev, V.V., A.A. Bagdasarov, E.L. Berezovsky, et al., *Plasma Physics Controlled Fusion* **30** (1988) 381.

Figure captions

Table

The table summarizes the results from regression analysis in the form $\text{param.} = \text{const.} \cdot A \alpha^{\pm \Delta \alpha} \cdot B \beta^{\pm \Delta \beta} \dots$. Independent parameters are current I_p , toroidal field B_t , density \bar{n}_e , Z_{eff} and the isotope mass A_i . In the column of dependent parameters, τ_E is global energy confinement time, τ_{SZ} is the sawtooth repetition time; the other parameters are given in the usual notation. The table lists the various exponents and their standard error; R is the regression coefficient.

- a Linear density range ($\bar{n}_e < 2.5 \times 10^{13} \text{ cm}^{-3}$); carbonized walls.
- b Saturated density range ($\bar{n}_e > 2.5 \times 10^{13} \text{ cm}^{-3}$); carbonized walls.
- c Saturated density range ($\bar{n}_e > 2.5 \times 10^{13} \text{ cm}^{-3}$); boronized walls.
In this case, Z_{eff} was low and did not change sufficiently with \bar{n}_e ; therefore, no regression was tried.
- d With neutral injection ($P_{\text{NI}} \approx 1.6 \text{ MW}$; $\bar{n}_e > 2.5 \times 10^{13} \text{ cm}^{-3}$); boronized walls.

Figure 1:

(a) Energy confinement time vs. density in the 3 confinement regimes LOC, SOC and IOC; τ_E^{kin} and τ_E^* are deduced from profile or diamagnetic measurements, respectively.

(b) Density dependence of the density profile shape parameter.

Figure 2:

Total-, electron-, and ion energy vs. density; Ohmic conditions.

Figure 3:

Separatrix temperature versus separatrix density for various Ohmic scenarios. (The code data and the theoretical data are increased by a factor of 2 in order to account for the 1 cm difference in nominal and measured separatrix position; see text.)

Figure 4

The left-hand-side of equation (6) as a function of power flow into the

scrape-off layer P_{sol} . $\bar{n}_e = 2$ (x), 3.5 (■), 5.5 (○) $\times 10^{13} \text{ cm}^{-3}$, $I_p = 320 \text{ kA}$, $B_t = 2.17 \text{ T}$. $P_{\text{NI}} = 0 - 1.8 \text{ MW}$. The points at the far left side for each density range arise from Ohmic heating.

Figure 5

The edge pressure for hydrogen and deuterium as a function of P_{sol} for the ohmically-heated boronized-wall case. The P_{sol} scan is achieved by varying $I_p = 250 - 450 \text{ kA}$, $B_t = 1.9 - 2.8 \text{ T}$ and $\bar{n}_e = 2.5 - 6 \times 10^{13} \text{ cm}^{-3}$.

Figure 6

Temporal evolution of various plasma parameters during three IOC test discharges under different wall conditions. Q_n is the ratio of the line-integrated density as measured with two interferometer channels: $Q_n = n_e(0) / n_e(0.75a)$. #24707 with uncovered stainless steel walls gives a typical IOC transition. #30451 with boronized walls remains in the SOC regime. #30687 with boronized walls has additional neon puffing during $0.5 - 0.8 \text{ s}$ and with a more intense puff between $1.5 - 1.9 \text{ s}$.

Figure 7:

Power input into the SOL for three different density plateaus (2.7 , 4.0 , and $5.4 \times 10^{13} \text{ cm}^{-3}$) of a hydrogen and the three IOC test discharges of Figure 6.

Figure 8:

Correlation between energy confinement time and density for the three IOC test discharges of Figure 6 during the time interval $0.5 - 2.5 \text{ s}$.

Figure 9:

Temporal evolution of the power into the SOL during the three IOC test discharges of Figure 6.

Figure 10

Neutron rate as a function of line-averaged density for Ohmic discharges with different wall conditioning and impurity injection.

Figure 11

Temporal evolution of the separatrix temperature during the three IOC test discharges of Figure 6.

Figure 12

Temporal evolution of the radial location of the stability parameter $\eta_e = L_{ne}/L_{Te} = 1.5$ for the three IOC test discharges of Figure 6. The region between the plasma boundary and the curve plotted has values with $\eta_e < 1.5$.

Figure 13

Experimental values of total energy, Ohmic power and energy confinement time versus the results from the regression analysis.

Figure 14

Total energy content versus plasma current for Ohmic plasmas and beam heated ones at 3 power levels (0.4, 0.8, and 1.6 MW). The results are shown for cases where the current was slowly ramped up during the beam pulse (continuous data) or for scans at various steady state current levels. Apart from the OH case, the data indicate an offset-linear relation.

Figure 15

Ohmic heating power versus density for various plasma currents. For the 250 kA case data points and fit-curve are shown. For the other cases the fit-curves only are given.

const	Ip	Bt	ne	Zeff	Ai	R
-------	----	----	----	------	----	---

a

Poh	9.93E-04	1.02	0.04	-0.45	0.07	0.26	0.05	0.24	0.05	-0.09	0.03	0.96
Wtot	2.43E-02	1.12	0.04	-0.18	0.07	0.56	0.05	-0.14	0.05	0.21	0.03	0.97
We	1.69E-02	1.12	0.04	0.00	0.00	0.38	0.05	-0.11	0.05	0.18	0.03	0.97
τ E	3.73E+01	0.00	0.00	0.27	0.11	0.39	0.06	-0.28	0.06	0.31	0.04	0.80
Teo	4.13E+01	0.49	0.05	0.73	0.09	-0.36	0.06	0.14	0.06	0.24	0.03	0.88
<Te>	6.14E+00	0.77	0.04	0.21	0.08	-0.37	0.05	0.12	0.05	0.17	0.03	0.92
Teo/<Te>	6.83E+00	-0.27	0.04	0.51	0.11	0.00	0.00	0.00	0.00	0.00	0.00	0.54
neo	4.02E+00	-0.14	0.03	0.00	0.00	0.85	0.03	-0.25	0.03	0.02	0.00	0.97
<ne>	2.31E-01	0.33	0.04	-0.17	0.08	0.68	0.05	-0.25	0.05	-0.12	0.03	0.93
neo/<ne>	1.49E+01	-0.46	0.03	0.24	0.07	0.16	0.03	0.00	0.00	0.20	0.03	0.83
Tio	5.75E+01	0.40	0.03	0.36	0.07	0.10	0.03	0.00	0.00	0.00	0.00	0.81
τ SZ	5.64E+01	-0.43	0.08	0.00	0.00	0.81	0.06	0.00	0.00	0.25	0.06	0.83
Zeff	2.03E-01	0.56	0.04	0.00	0.00	-0.82	0.04	0.00	0.00	0.00	0.00	0.86
Wi	3.83E-03	1.37	0.18	0.00	0.00	0.54	0.23	-1.11	0.23	0.13	0.00	0.76
Tio/Teo	9.08E-01	0.00	0.00	-0.35	0.07	0.35	0.03	-0.22	0.03	-0.22	0.03	0.88

b

Poh	7.93E-04	1.09	0.03	-0.40	0.06	0.24	0.04	0.00	0.00	-0.22	0.03	0.96
Wtot	5.74E-02	0.99	0.03	-0.13	0.06	0.43	0.05	-0.16	0.05	0.28	0.03	0.97
We	1.40E-02	1.14	0.03	0.00	0.00	0.35	0.04	0.00	0.00	0.27	0.03	0.97
τ E	5.76E+01	0.00	0.00	0.18	0.07	0.00	0.00	-0.27	0.05	0.50	0.03	0.86
Teo	1.53E+02	0.31	0.03	0.79	0.06	-0.63	0.04	0.00	0.00	0.36	0.02	0.94
<Te>	5.92E+00	0.84	0.05	0.19	0.09	-0.62	0.06	0.00	0.00	0.19	0.04	0.88
Teo/<Te>	5.62E+01	-0.67	0.04	0.66	0.07	0.00	0.00	0.00	0.00	0.11	0.03	0.87
neo	4.66E+00	-0.21	0.03	0.14	0.06	0.84	0.04	-0.11	0.04	0.10	0.02	0.93
<ne>	9.68E-02	0.42	0.03	-0.26	0.06	1.01	0.04	-0.10	0.04	-0.12	0.02	0.97
neo/<ne>	3.73E+01	-0.59	0.03	0.37	0.05	-0.17	0.03	0.00	0.00	0.25	0.02	0.94
Tio	1.13E+02	0.29	0.05	0.55	0.09	-0.28	0.07	0.00	0.00	0.16	0.04	0.72
τ SZ	1.57E+01	0.00	0.00	0.00	0.00	0.00	0.00	-0.61	0.08	0.54	0.05	0.82
Zeff	3.86E+00	0.00	0.00	-0.42	0.13	-0.28	0.08	0.00	0.00	0.00	0.00	0.39
Tio/Teo	7.10E-01	0.00	0.00	-0.26	0.08	0.31	0.05	0.00	0.00	-0.21	0.04	0.66

	const	lp	Bt	ne	Zeff	Ai	R
--	-------	----	----	----	------	----	---

C

Poh	5.62E-04	1.13	0.02	-0.35	0.03	0.26	0.02	-0.18	0.01	0.99
Wtot	1.55E-02	1.19	0.04	-0.32	0.07	0.44	0.05	0.47	0.03	0.98
We	1.32E+02	1.17	0.01	0.00	0.00	0.44	0.02	0.36	0.01	1.00
τE	3.80E+01	0.00	0.00	0.00	0.00	0.21	0.05	0.65	0.04	0.92
Teo	1.35E+02	0.29	0.02	0.72	0.03	-0.50	0.03	0.33	0.02	0.97
<Te>	2.34E+00	0.96	0.02	0.00	0.00	-0.55	0.03	0.29	0.02	0.98
Teo/<Te>	5.75E+01	-0.66	0.03	0.68	0.05	0.00	0.00	0.05	0.02	0.95
neo	2.57E+00	-0.13	0.01	0.18	0.02	0.91	0.02	0.08	0.01	0.99
<ne>	1.91E-01	0.27	0.03	0.00	0.00	0.98	0.04	-0.12	0.02	0.97
neo/<ne>	1.12E+01	-0.40	0.03	0.28	0.05	0.08	0.04	0.17	0.02	0.90
Tio	3.55E+02	0.17	0.04	0.35	0.06	-0.42	0.04	0.00	0.00	0.79
τSZ	1.20E+02	-0.48	0.09	0.00	0.00	0.27	0.11	0.44	0.07	0.71

d

Wtot	2.40E-01	0.87	0.02	-0.14	0.04	0.14	0.02	0.44	0.03	0.98
We	5.25E-02	0.88	0.02	0.09	0.03	0.52	0.02	0.24	0.01	0.99
τE	1.10E+00	0.55	0.03	-0.14	0.04	0.09	0.03	0.34	0.02	0.94
Teo	2.63E+02	0.27	0.03	0.55	0.05	-0.46	0.04	0.25	0.02	0.88
<Te>	6.61E+00	0.83	0.02	0.11	0.03	-0.49	0.02	0.13	0.01	0.97
Teo/<Te>	3.98E+01	-0.56	0.03	0.44	0.05	0.00	0.00	0.12	0.02	0.90
neo	1.45E+00	0.00	0.00	0.09	0.02	0.90	0.01	0.07	0.01	0.99
<ne>	5.13E-01	0.08	0.02	-0.06	0.02	1.11	0.02	-0.15	0.01	0.99
neo/<ne>	2.82E+00	-0.11	0.02	0.14	0.03	-0.21	0.02	0.22	0.01	0.88
τSZ	1.10E+01	0.15	0.07	0.23	0.11	-0.39	0.07	0.46	0.04	0.72

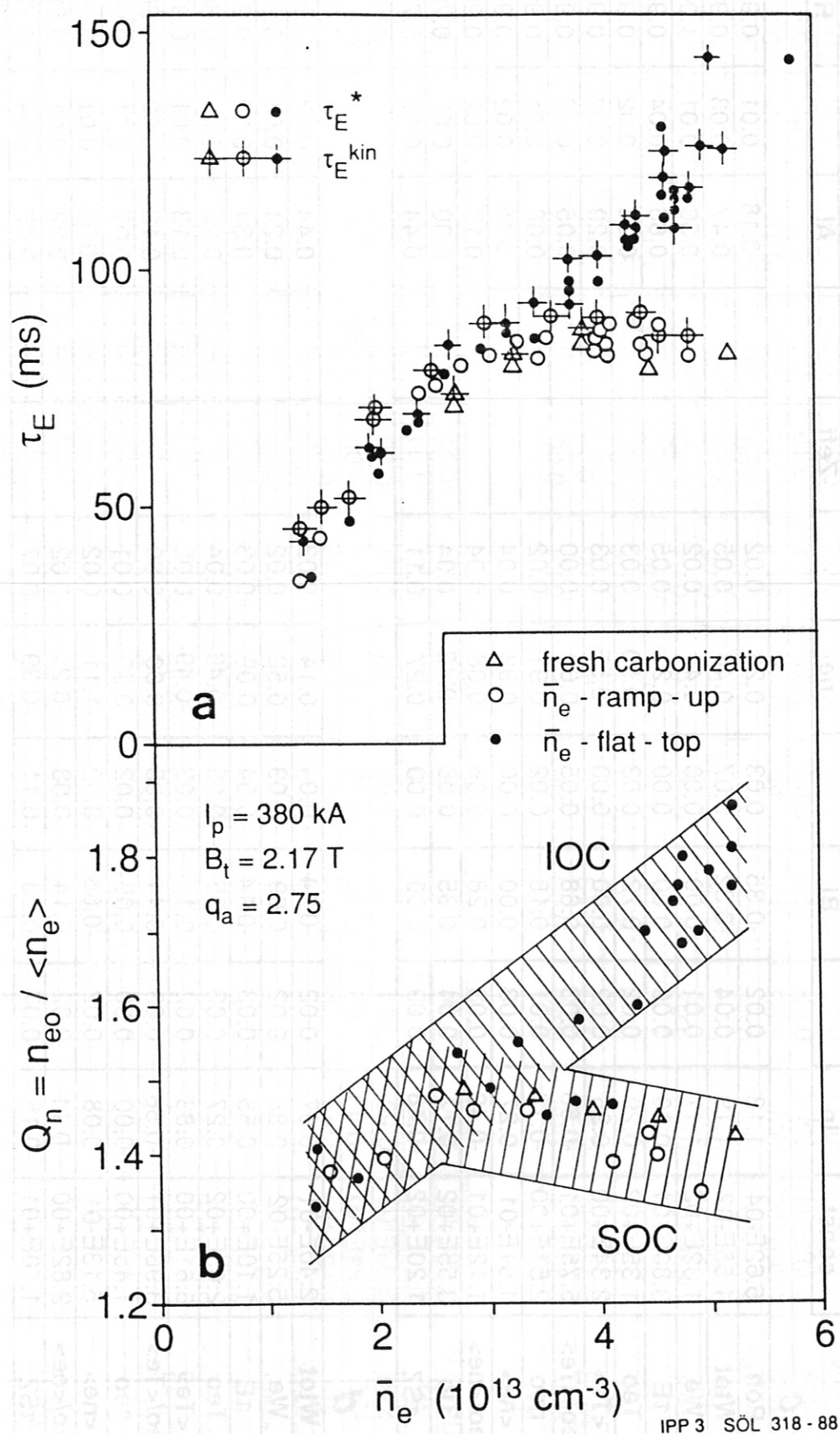


Figure 1

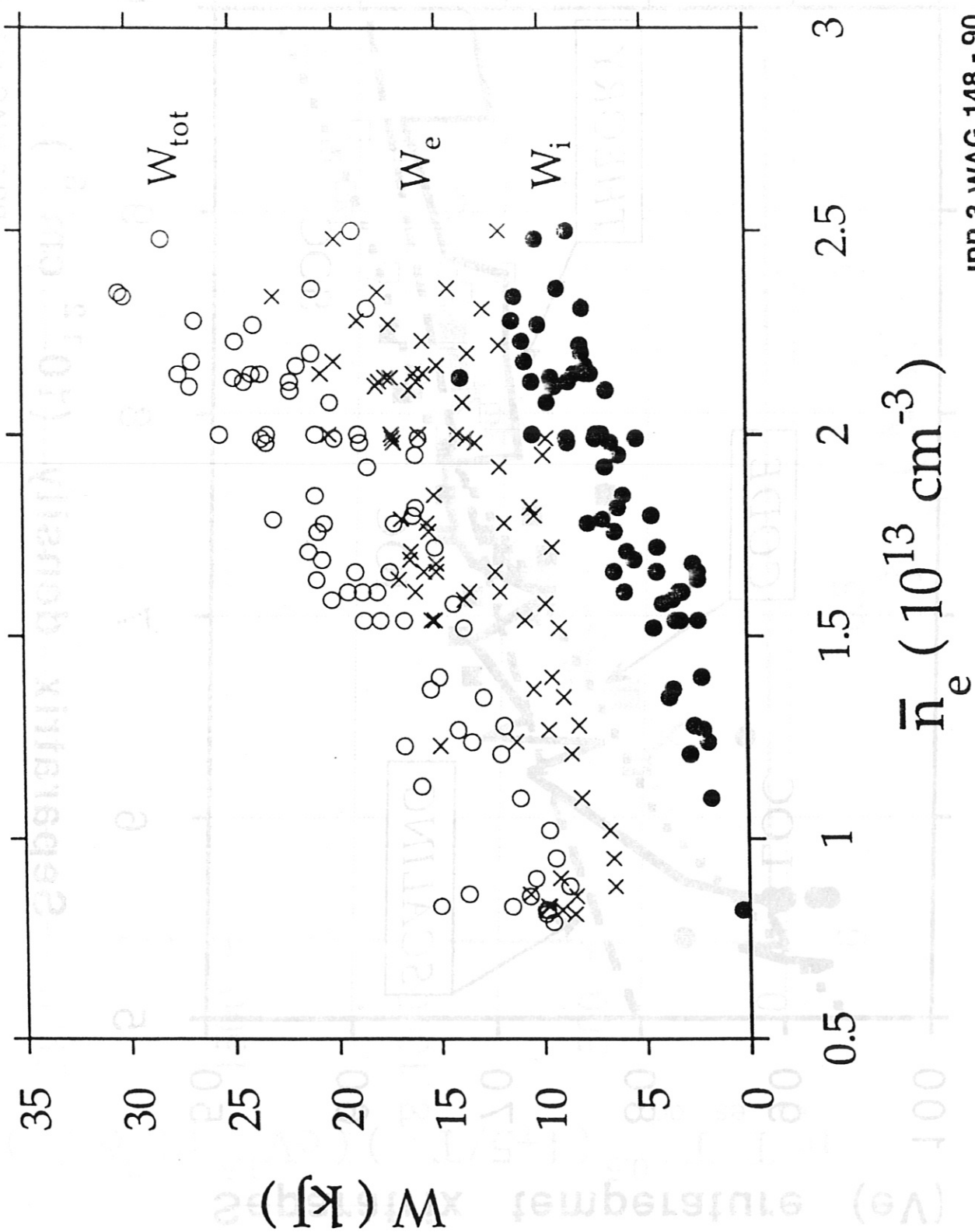
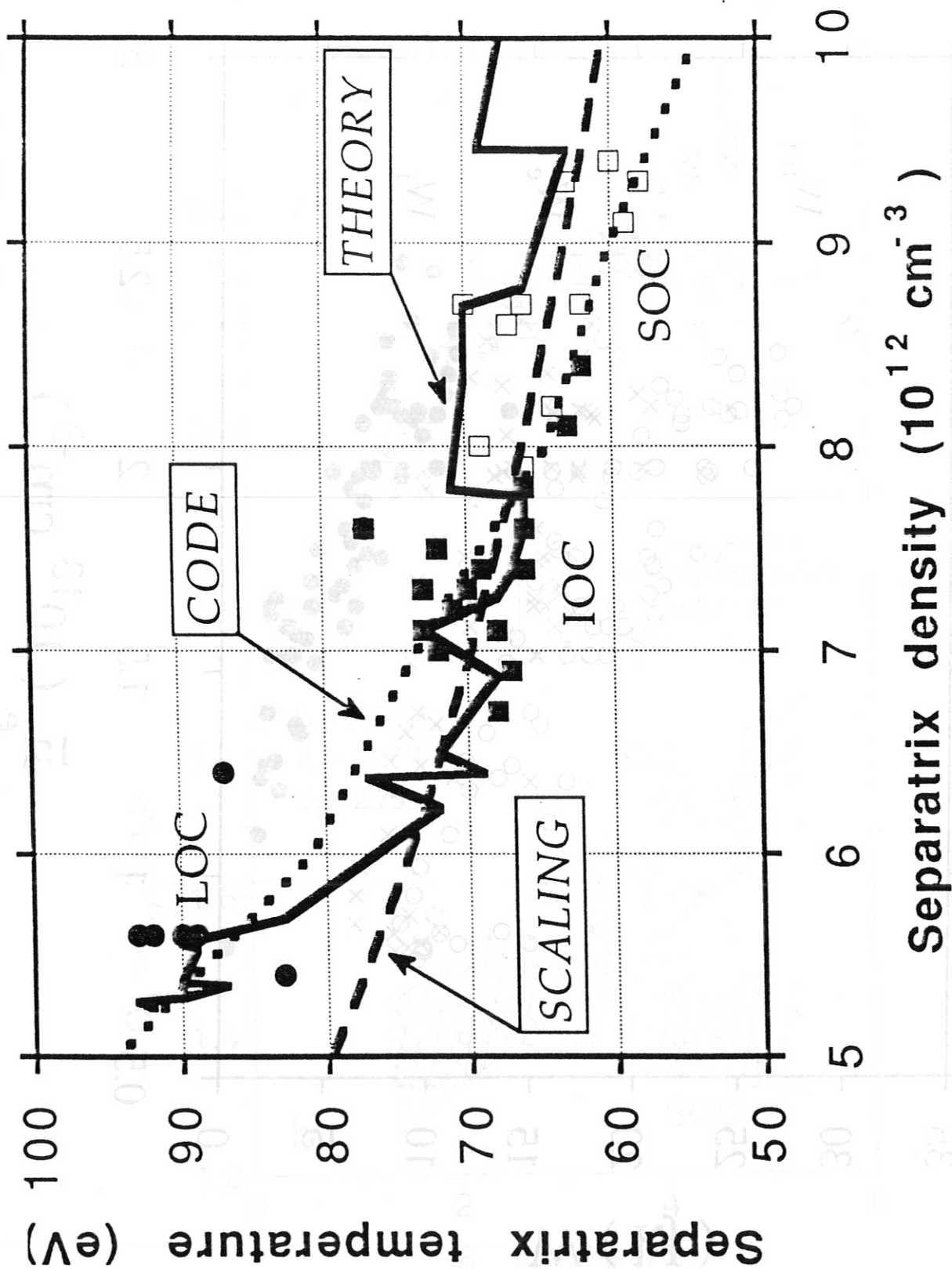


Figure 2



IPP 3 WAG 146 - 90

Figure 3

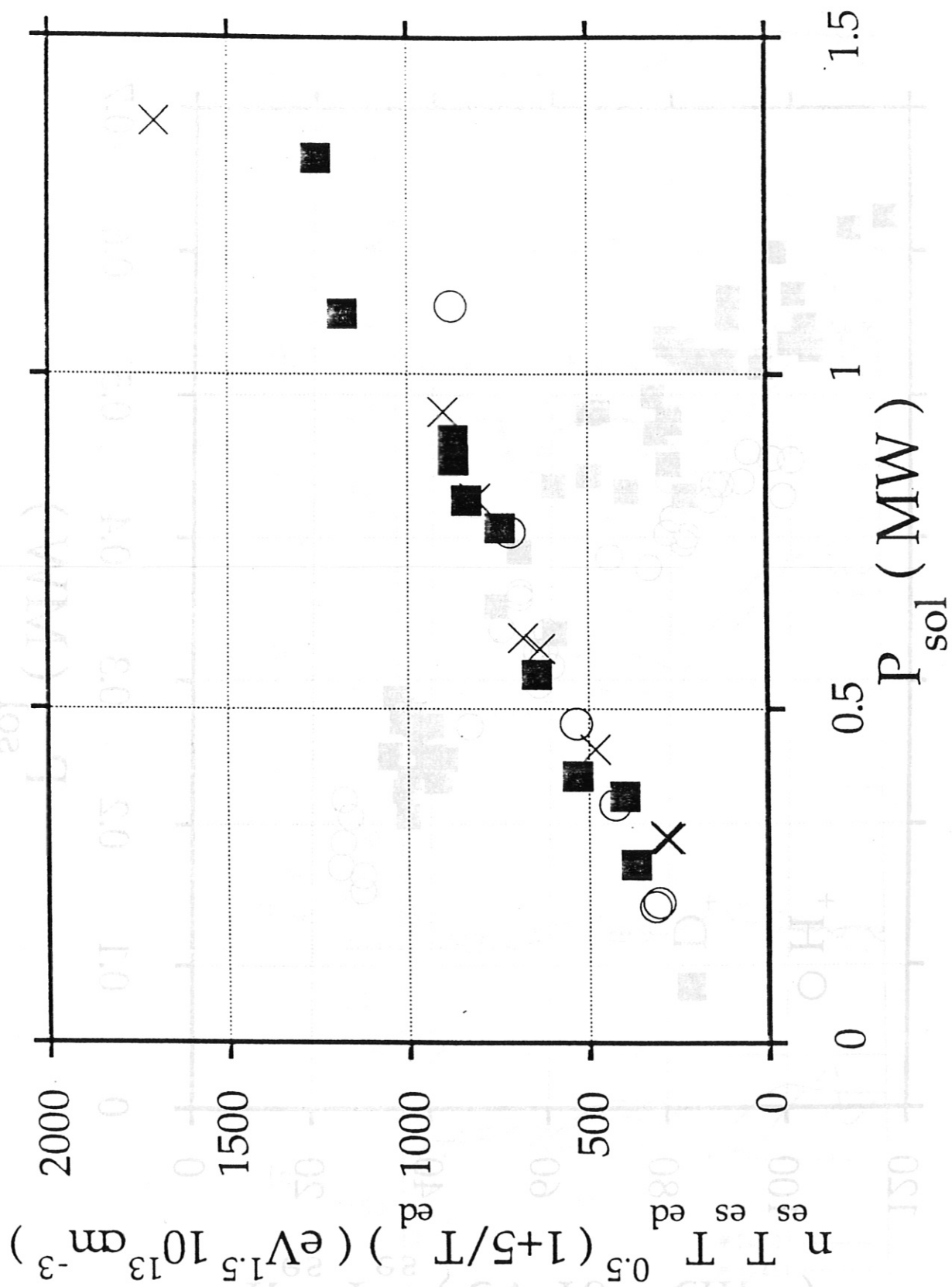
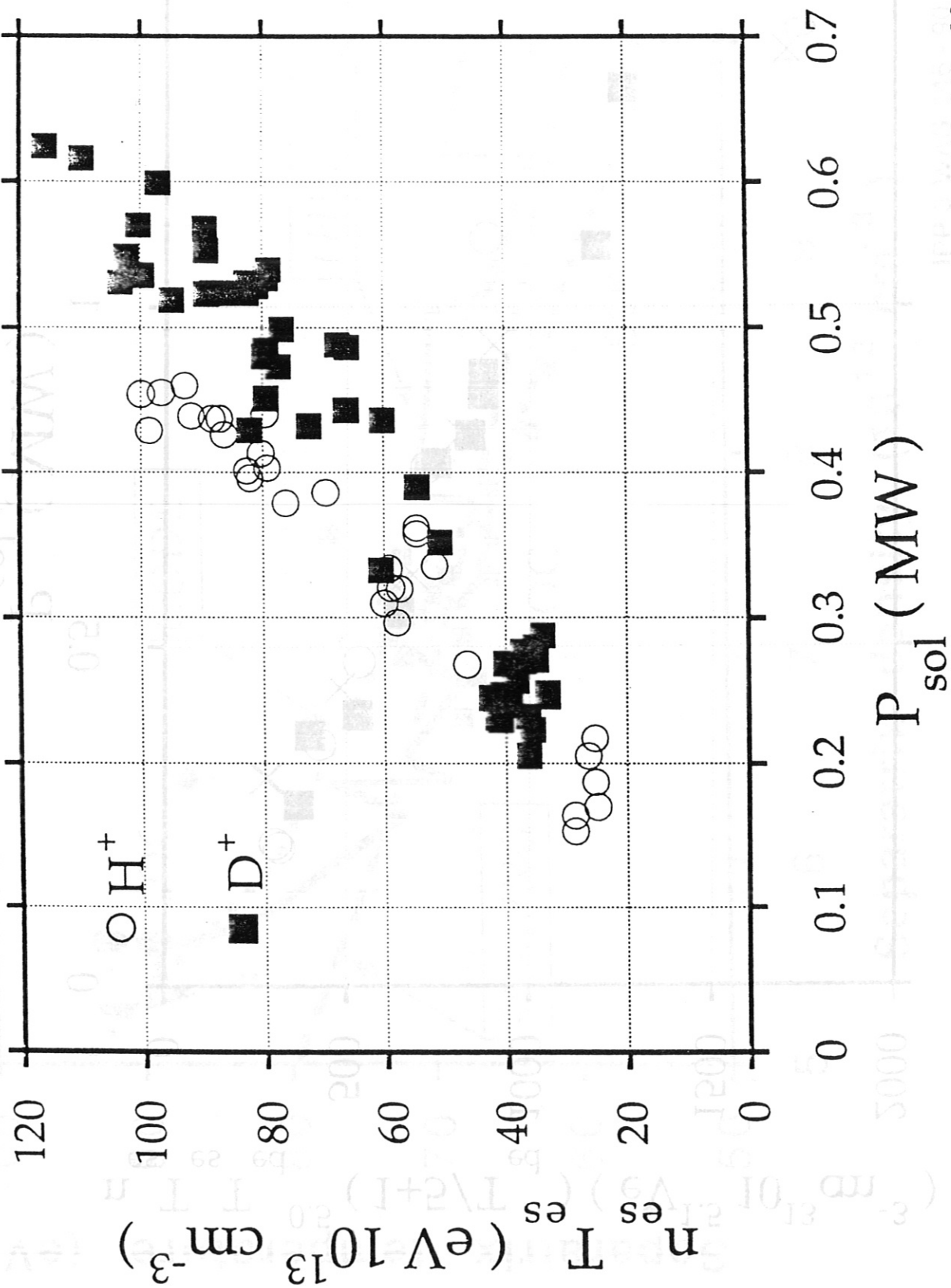
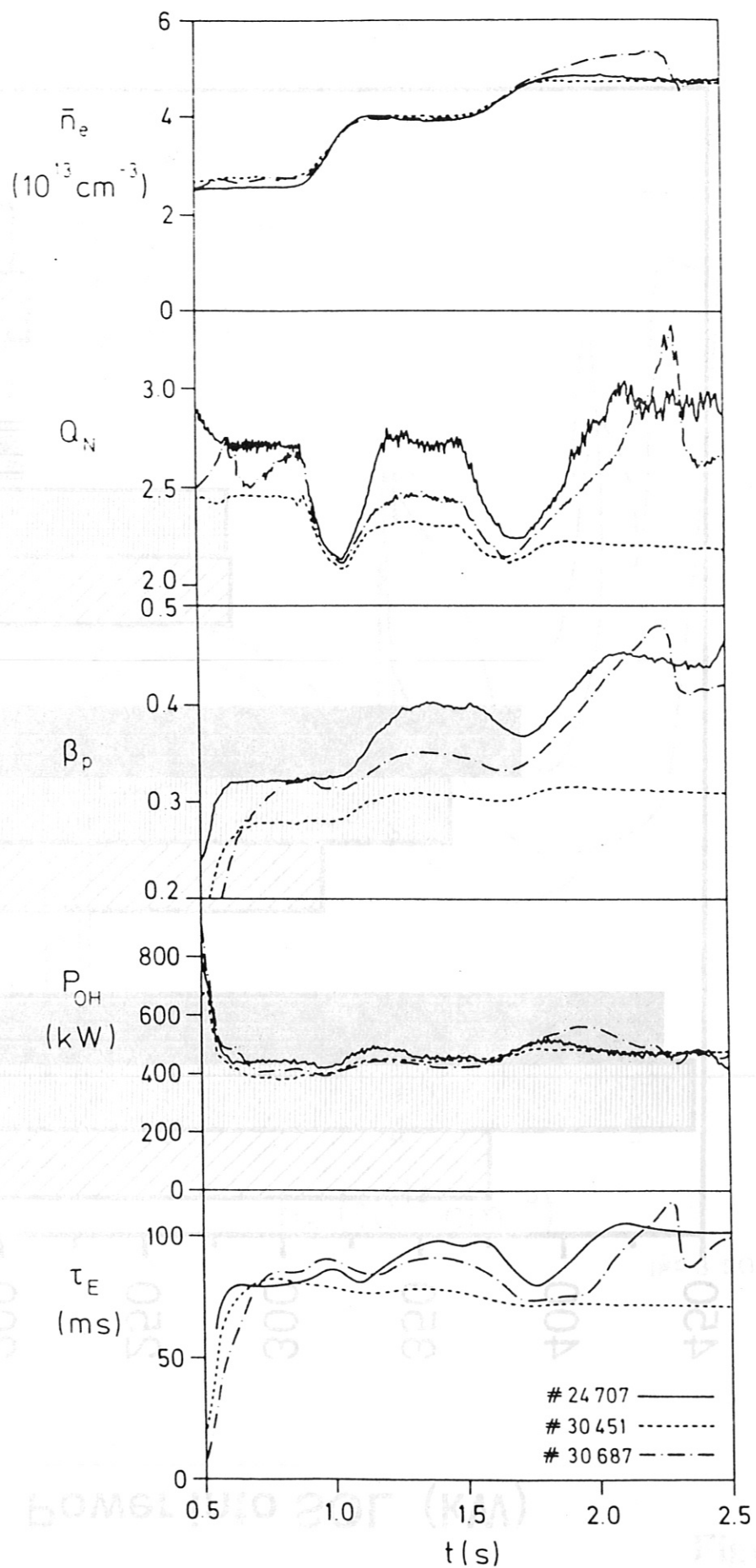


Figure 4



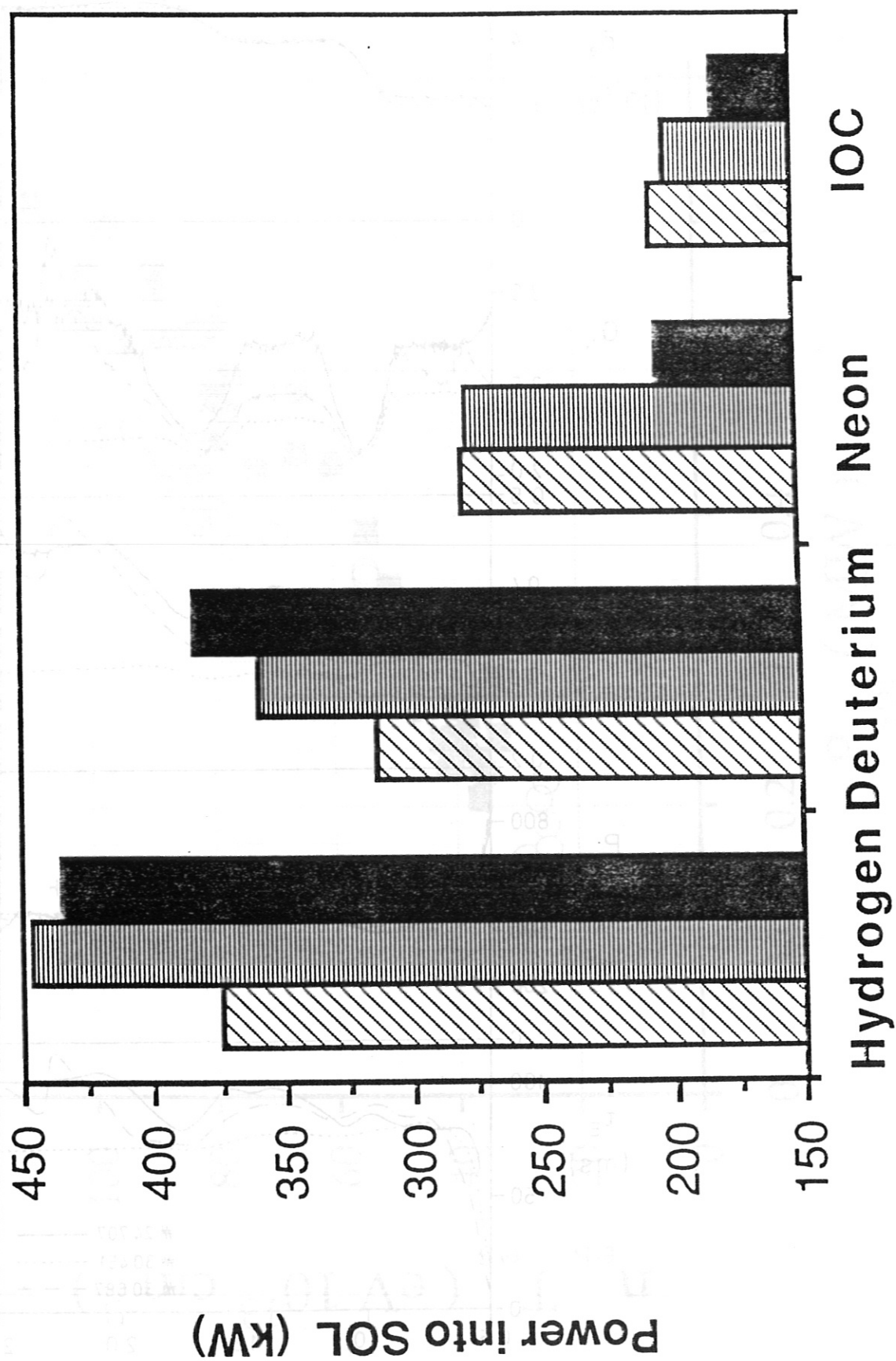
IPP 3 WAG 144 - 90

Figure 5



IPP 3 SOL 112-90

Figure 6

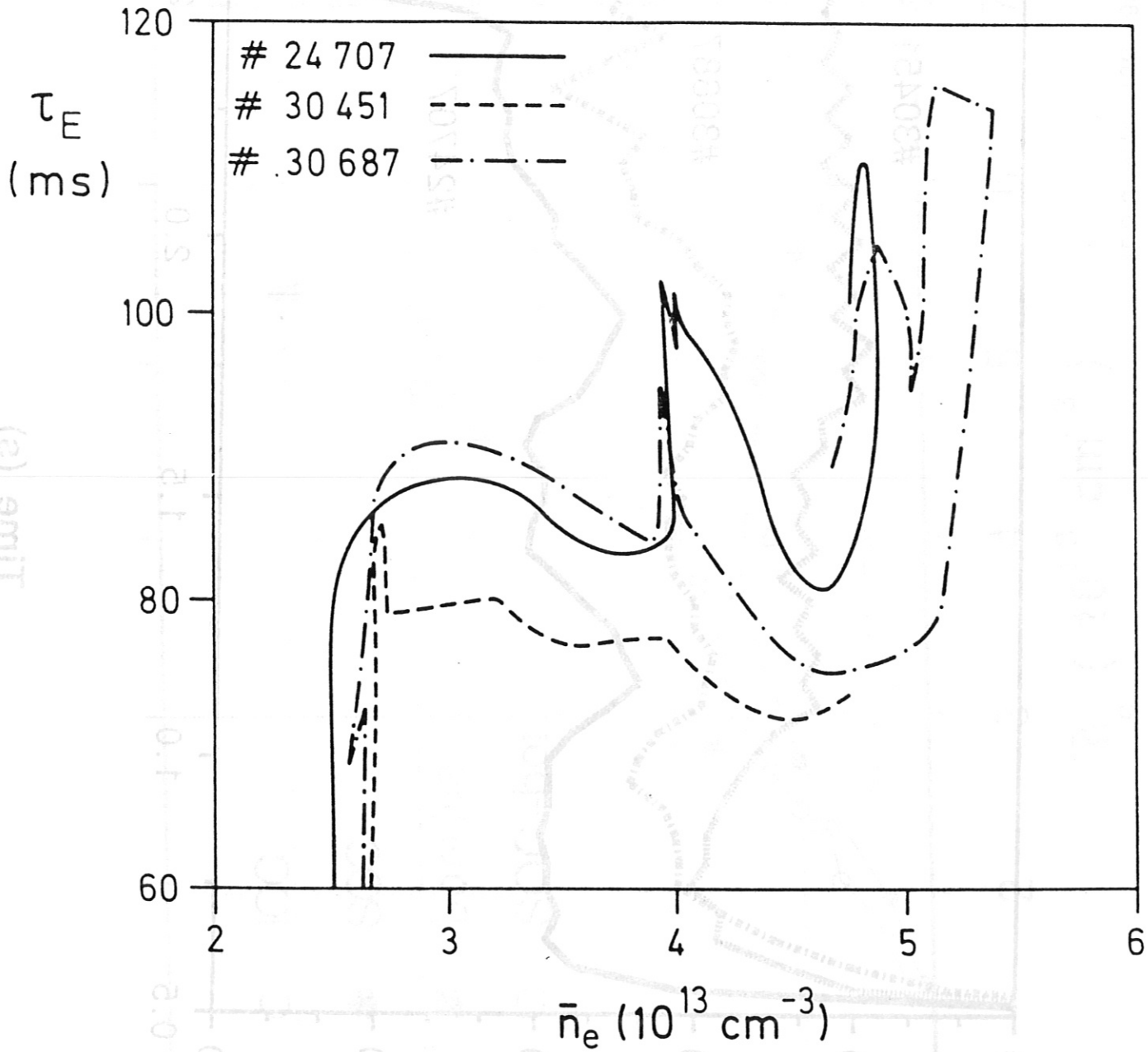


IPP 3 WAG 143 - 90

Figure 7

IPP 3 SOL 109-90

time (s)

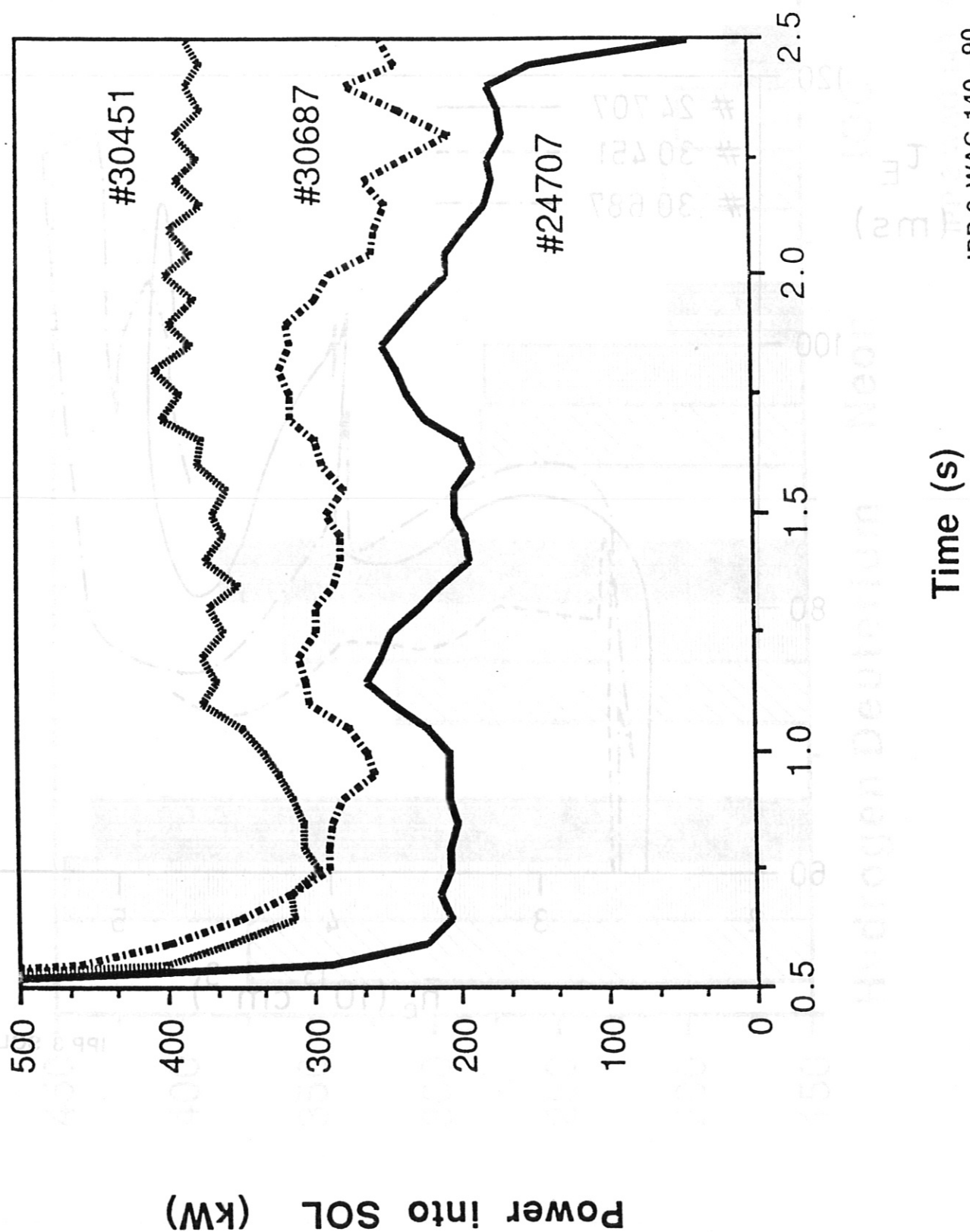


IPP 3 SOL 109 - 90

Figure 8

Figure 9

Figure 10



IPP 3 WAG 140 - 90

Figure 9

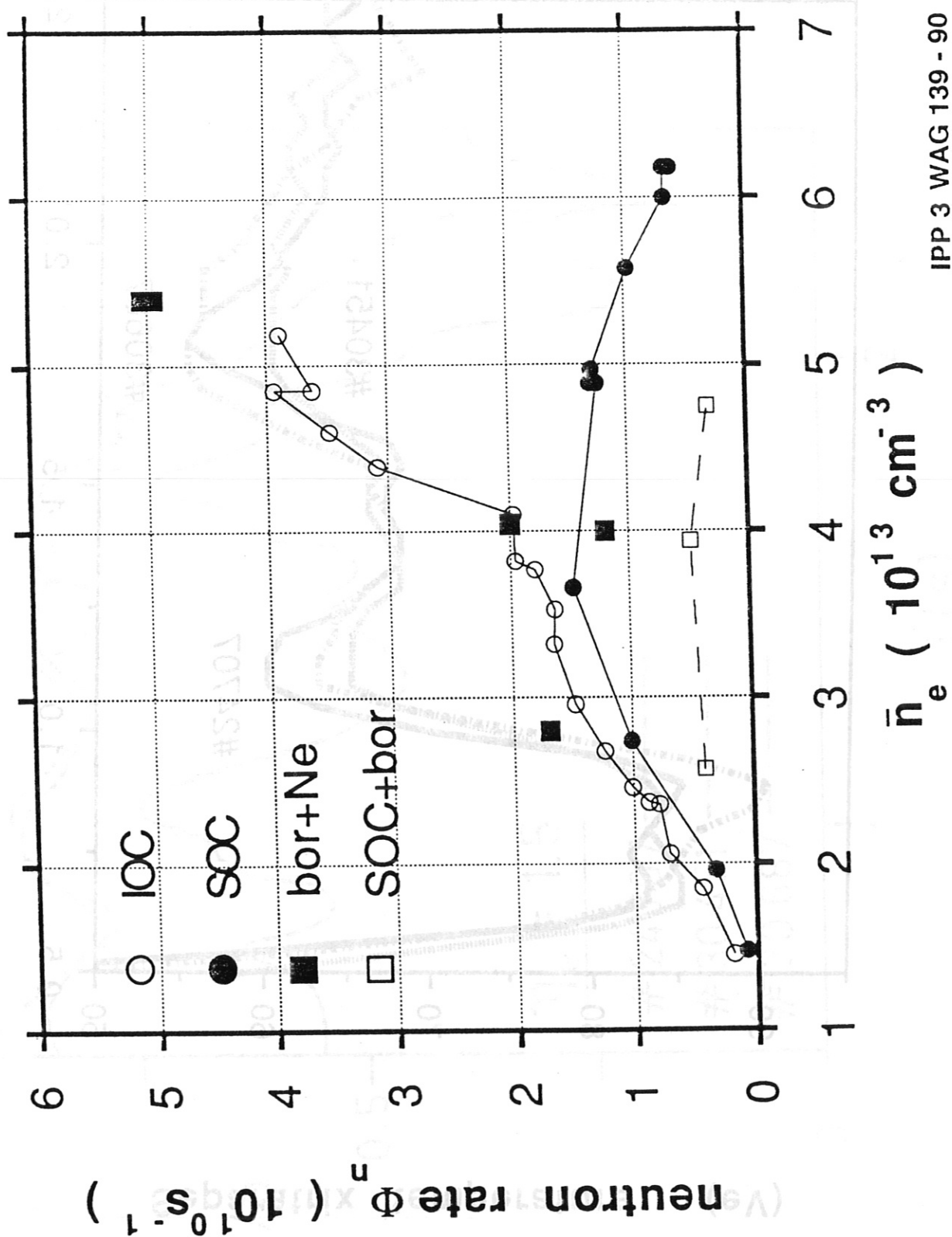


Figure 10

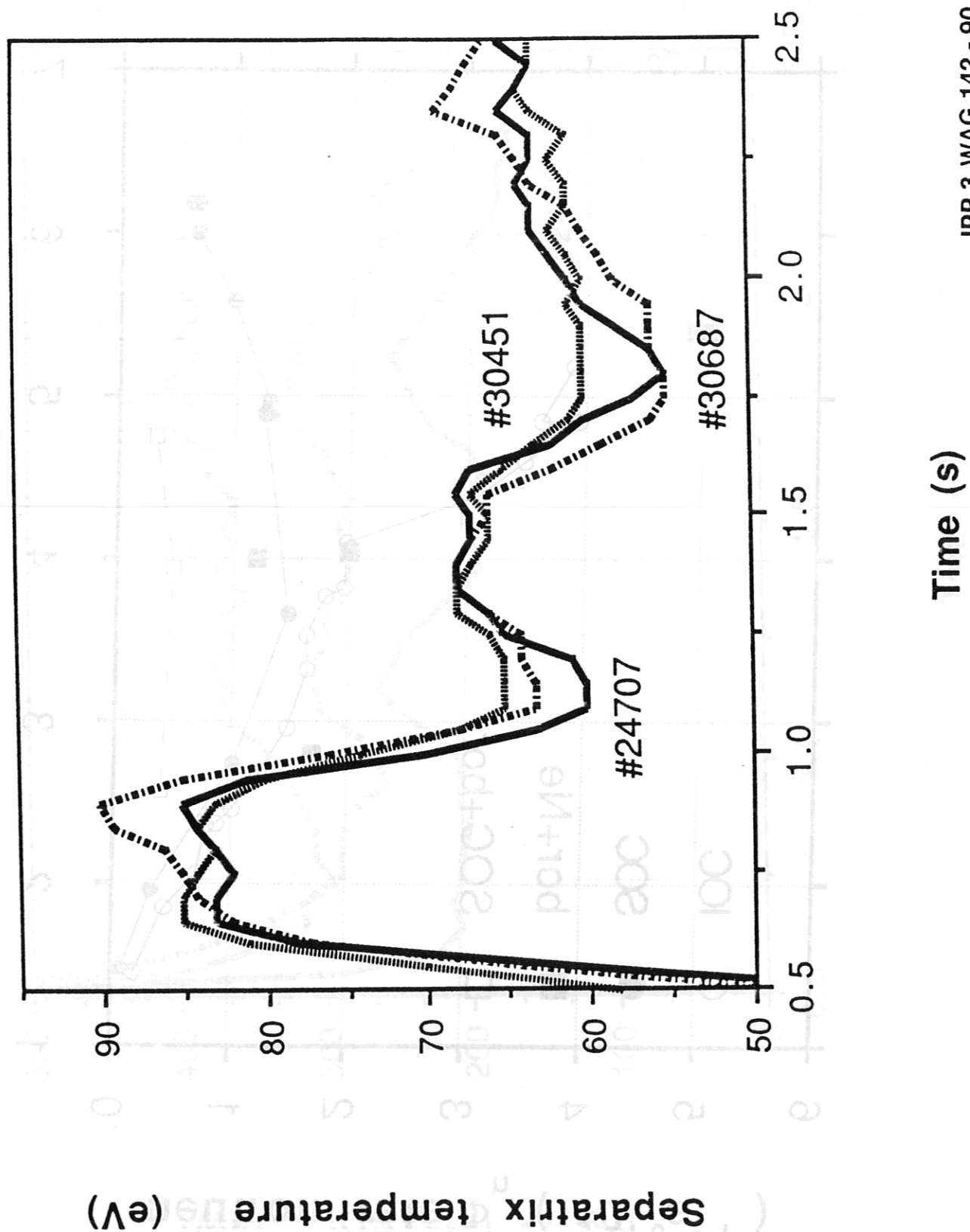


Figure 11

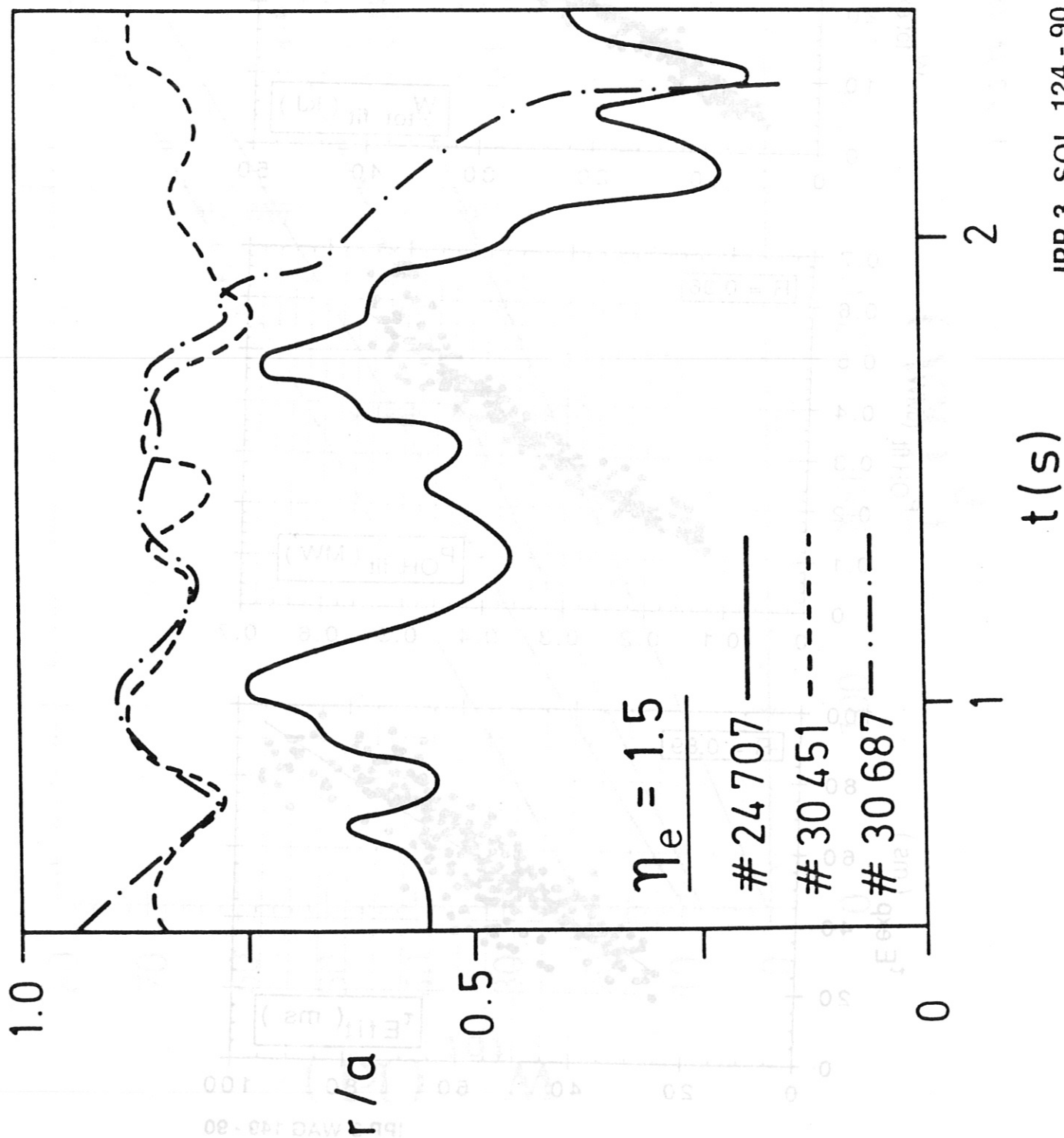


Figure 12

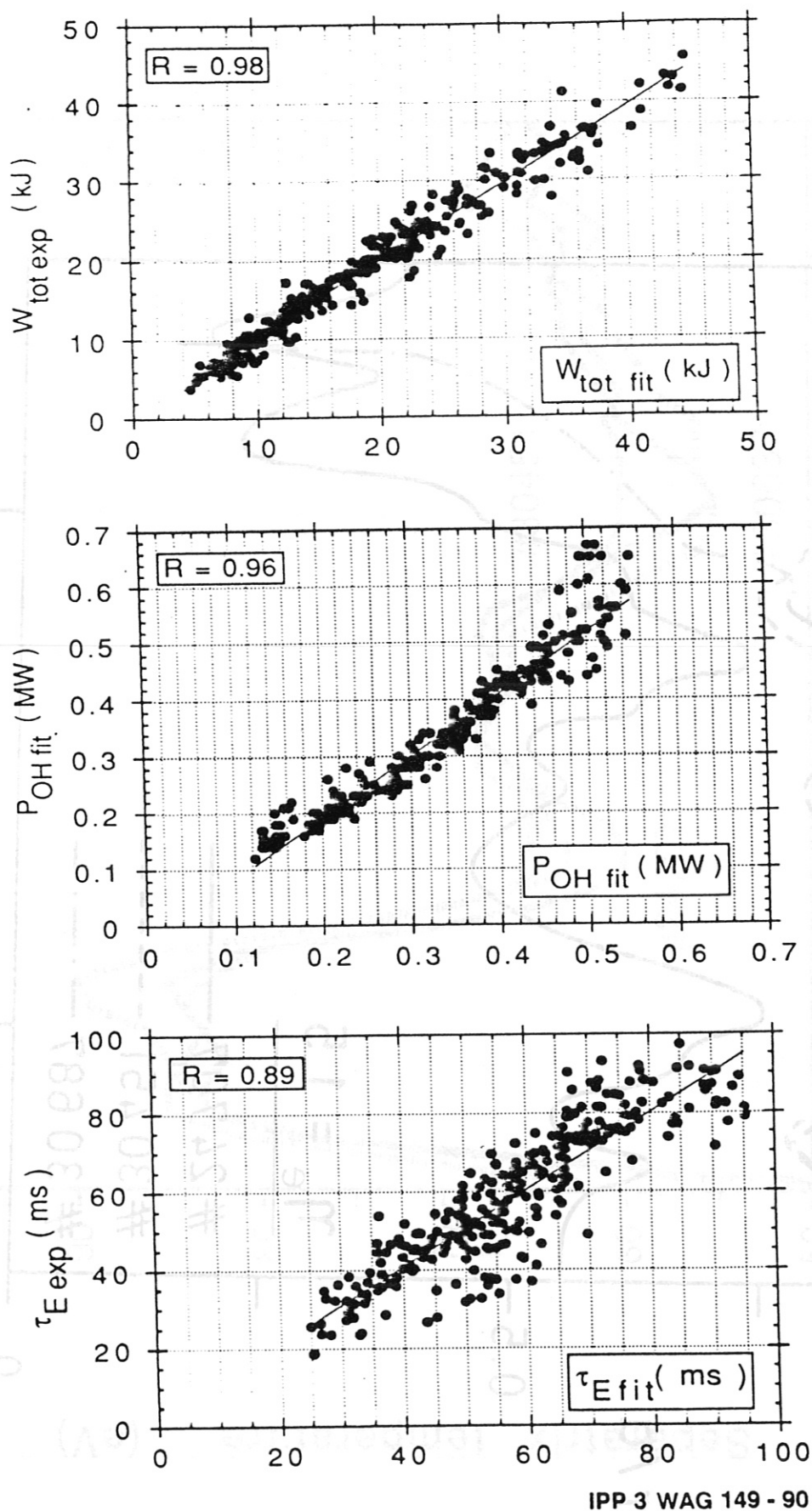
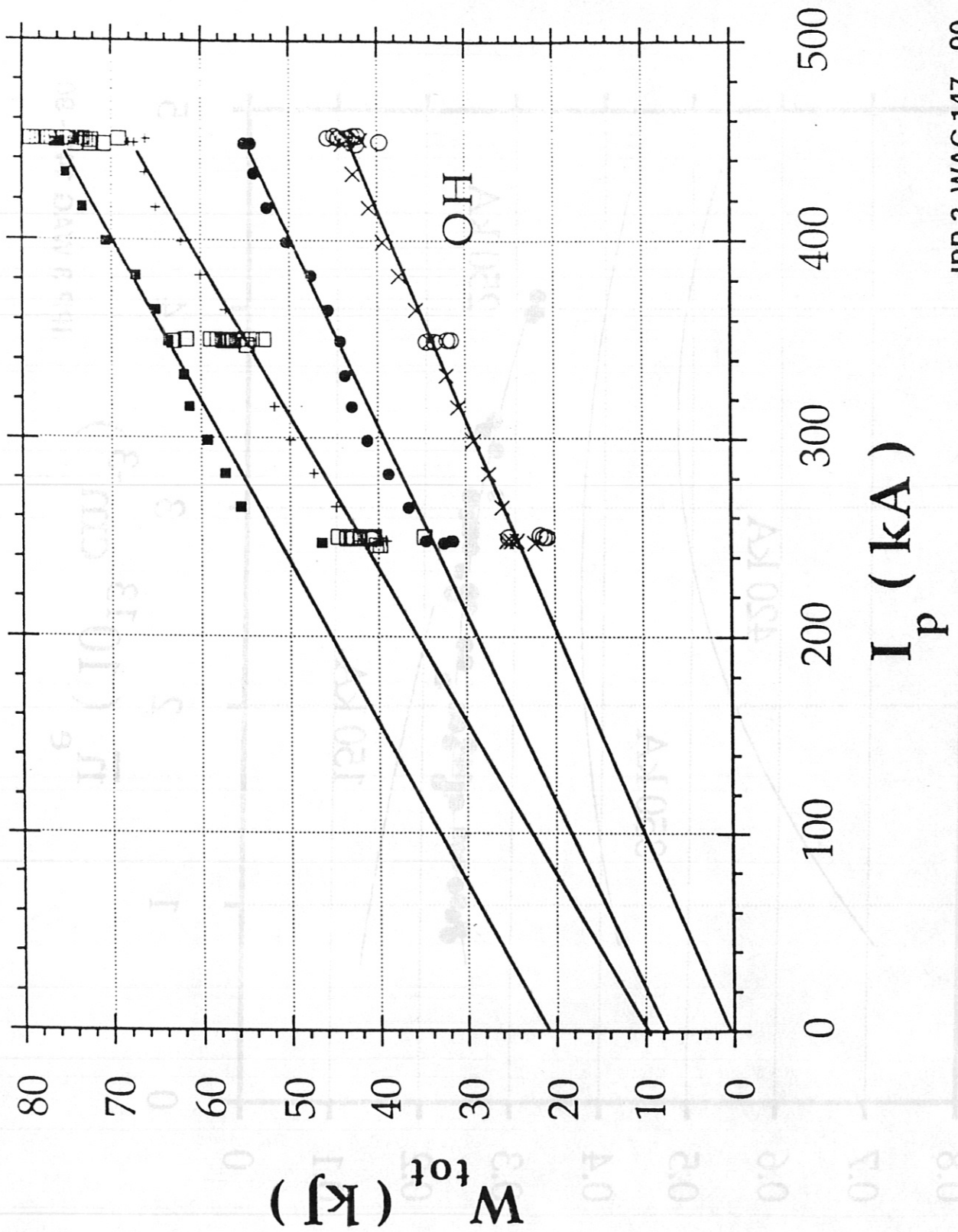
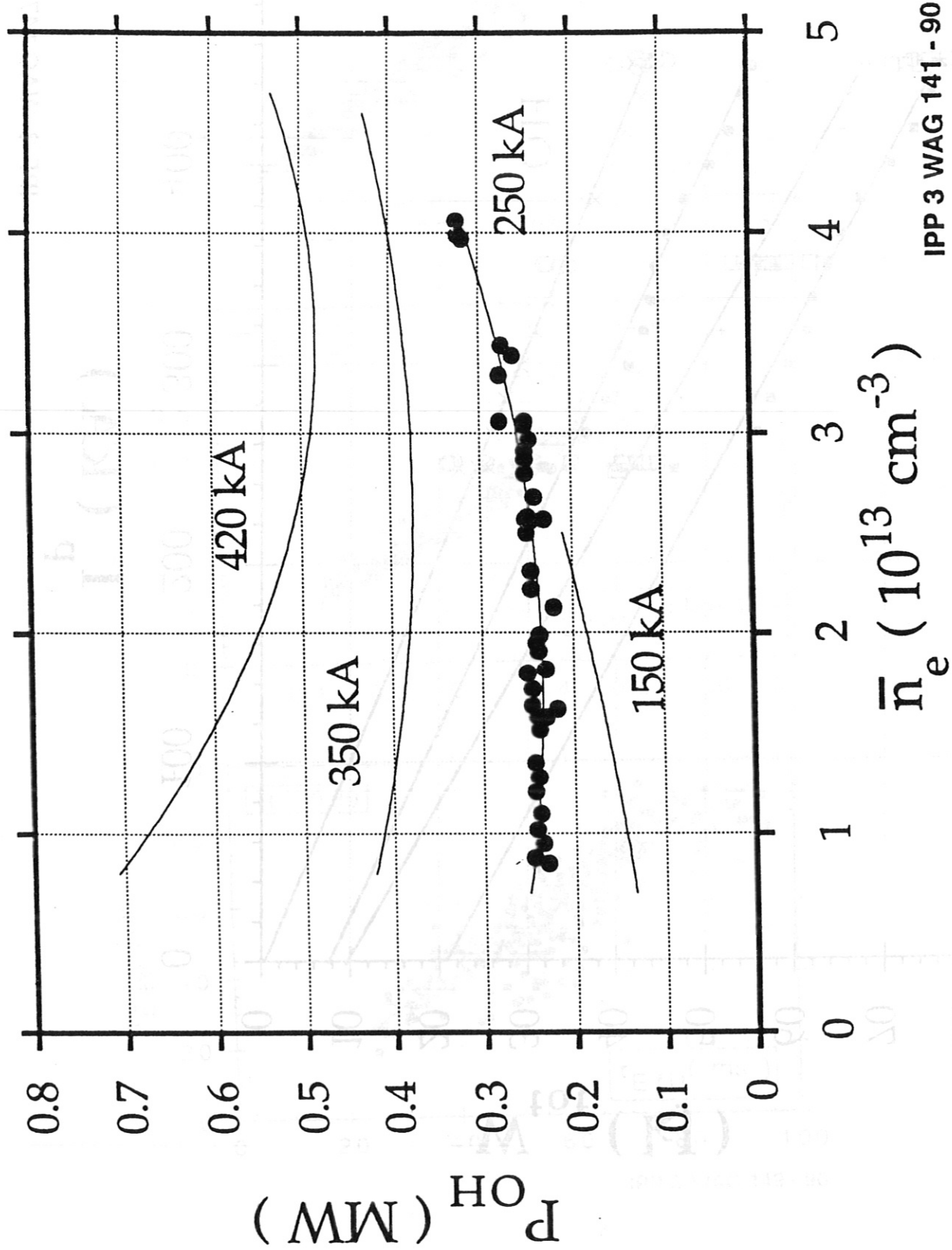


Figure 13



IPP 3 WAG 147 - 90

Figure 14



IPP 3 WAG 141 - 90

Figure 15